Passive Infrared Detection of Microburst Induced Low Level Wind Shear

by
Jim M. Staley

Department of Atmospheric Science
Colorado State University
Fort Collins, Colorado

Principal Investigator: Peter C. Sinclair

Colorado State University

Department of Atmospheric Science

Paper No. 467

PASSIVE INFRARED DETECTION OF MICROBURST INDUCED

LOW LEVEL WIND SHEAR

.

by

Jim M. Staley

Department of Atmospheric Science
Colorado State University
Fort Collins, CO 80523

PASSIVE INFRARED DETECTION OF MICROBURST INDUCED LOW LEVEL WIND SHEAR

During the past two decades the aviation community has come to recognize the microburst (Fujita, 1985), as an extreme hazard to aviation. When an aircraft encounters a microburst during the critical landing or takeoff stages, a strong head-wind to tail-wind shear is experienced along with a coupled severe downdraft. If the shear is severe enough, the aircraft may crash due to loss of lift. In a effort to provide ample warning time of a possible microburst encounter, the Federal Aviation Administration is spearheading research and development of microburst detection and warning systems. Surface anemometer networks and customized Doppler radars, among other systems, are currently being evaluated exclusively for detection of these hazardous microbursts.

The purpose of this work is to determine theoretically, the microburst detection capabilities of a passive infrared (IR) radiometer system. The proposed system detects a cold microburst based on its temperature difference as compared to the ambient environmental temperature. Also, a ranging technique (employing weighting functions) is examined. This ranging scheme is similar to that proposed by Caracena, *et al.*, (1981),Kuhn, *et al.* (1983), Kuhn and Kurkowski (1984), and utilized by Sinclair and Kuhn (1990) to estimate the location of a given microburst.

Also included in this study is a general overview of atmospheric transmission characteristics as applied to the infrared 12.5 - 15μ portion of the electromagnetic spectrum. This part of the spectrum seems well suited for this microburst application and contains only two significant atmospheric absorbers; CO_2 and atmospheric water vapor.

ii

Various microburst atmospheres are modeled using a customized application of the radiative transfer equation. These modeled atmospheres are divided into two categories: (1) High Plains or relatively "dry" boundary layers and (2) south-east United States systems that are characteristically more water saturated than the high plains enviornment. Radiance and transmission calculations are accomplished using the Air Force Geophysics Laboratory code FASCOD2.

Model output results indicate that microbursts are detectable with currently available infrared sensors. However, due to water loading effects, further range determination studies are required in order to reliably determine actual microburst location ahead of the sensor.

ACKNOWLEDGEMENTS

TABLE OF CONTENTS

TABLE OF CONTENTS

LIST OF FIGURES

Chapter 1

INTRODUCTION

As described by Fujita (1985), and Fujita (1986), the atmospheric microburst (MB) phenomena is an extreme hazard to aircraft safety. When an aircraft encounters a microburst, low level wind shear (LLWS) can reduce the amount of lift to a value below that required to keep the plane flying. If the encounter is close enough to the ground, a crash may occur.

Various methods are currently being evaluated to provide advanced warning of these downbursts. Doppler radar networks and gridded wind sensors are presently being used at many airports throughout the nation. These systems have proven effective in determining the presence of microbursts, but have several limitations. Often, these ground based systems do not provide good response time. A microburst warning may be received by the pilot after he is already committed to a landing. Also, many microbursts mature and dissipate in such a short period of time that ground based detection and dissemination by current means is not always timely.

An airborne microburst detector is needed. A low cost, low maintenance system that will provide real-time, accurate detection of this LLWS hazard. Having the detector "onboard" would provide a minimum amount of lag time between actual detection of the MB and the initiation of avoidance procedures by an aircrew.

Sinclair and Kuhn (1990) have shown experimentally that an airborne FLIR (Forward Looking Infrared) system can detect a microburst at a distance of 5- 10 km. One purpose of this thesis is to determine theoretically, the MB detection capabilities of a passive infrared (IR) radiometer system. Since microbursts are noticeably colder than their surrounding air, the system will be designed to measure the radiance difference between a MB and the ambient atmosphere.

An additional objective of this study is to analyze the MB ranging technique (employing weighting functions) developed by Caracena,*et al.* (1981),Kuhn,*et al.* (1983), Kuhn and Kurkowski (1984), and utilized by Sinclair and Kuhn (1990) to estimate the location of a given microburst. Any portion of the atmosphere (i.e. a MB) from which emitted radiation reaches a sensor depends on the molecular absorption characteristics of the intervening atmosphere for the wavelength of measurement. This absorption/transmission dependence will enable an IR detector to be most sensitive to radiance measurements at a distance where a pre-determined weighting function peaks in magnitude. Received radiant energy is interpreted in terms of the average temperature of this sensed portion of the atmosphere thru Planck's law.

This weighting function concept is by no means new and has practical application in present day remote sensing by satellite (Wark and Fleming, 1966 and Elachi, 1987). Satellite use of vertical weighting functions are heavily influenced by pressure broadening effects whereas in the horizontal, a constant pressure is implied. This makes our horizontal weighting functions appear more symmetric and well behaved than the horizontal variety.

A background on the microburst threat and microburst classification are presented in Chapter 2 along with an overview of current MB detection methods. Chapter 3 describes the physical scheme for a scanning radiometer as it "looks" at a given MB atmosphere. The remainder of the chapters examine the IR radiative properties and radiometric signatures of a microburst atmosphere.

In order to accomplish our objectives, a reduced form of Schwartzchild's equation is derived for use in the given MB scenario. We also conduct a preliminary study of atmospheric transmittance as required for use in this low altitude, horizontal 'look' application. Radiative calculations of our microburst atmosphere will enable us to determine the sensitivity of a FLIR system required to make these measurements. Likewise, our proposed ranging technique will be evaluated.

Sinclair and Kuhn, (1987) and Sinclair and Kuhn (1990) were able to conduct flight level MB penetration studies of high plains microbursts. Their data is used to help define our basic model input and represents most all of the available airborne data on this subject.

Accurate transmission values are necessary for the radiative transfer calculations utilizing Schwartzchild's equation. Presented in the Appendix are some current computational methods for determining atmospheric transmissivity and radiance. Among these methods are Air Force Geophysics Laboratory programs LOWTRAN7 and FASCOD2. These programs are used throughout this study and provide atmospheric transmissivity/radiance values used in our calculations.

Chapter 2

THE MICROBURST

The John F. Kennedy International Airport accident investigation by Fujita and Byers, (1977) documented the existence of strong, short-lived downdrafts that were not associated with large storms. These "microbursts" have been defined by Fujita as a strong downdrafts which create an outburst of damaging winds at or near the ground (Fujita, 1985). By Dr. Fujita's definition, damaging microburst winds have a surface horizontal extent of 4 kilometers or less, and were observed by Wilson, *et al.*, (1984) to last normally from 2 to 10 minutes. Even though a microburst is a small scale feature, an intense microburst (MB) may produce anomalous surface winds as high as 75 m/s ($\approx$ 150 kts), Figure 2.1
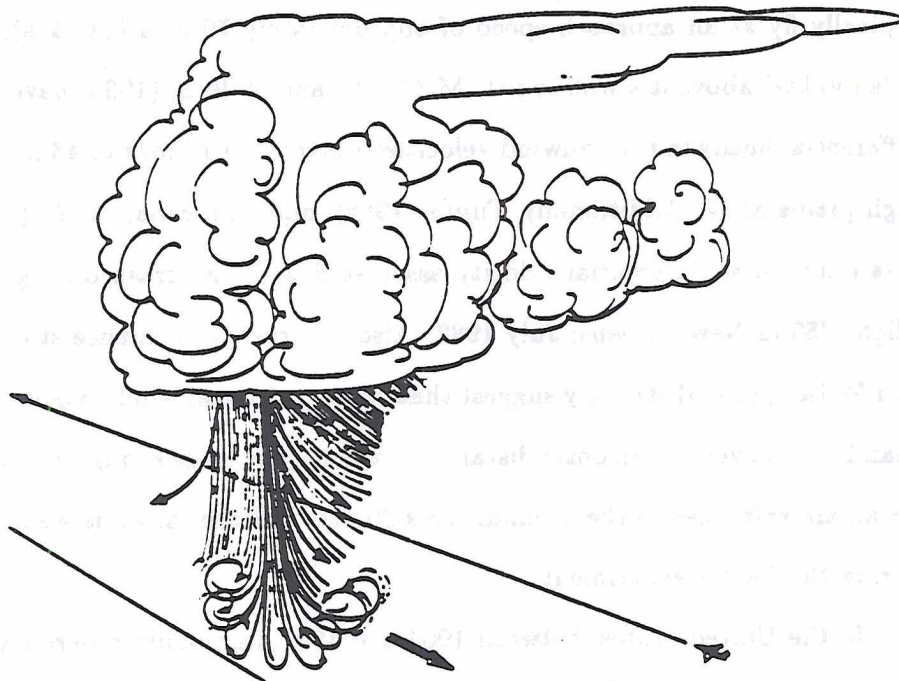
Figure 2.1: The Idealized Microburst   from Sinclair, (1990)

Most of the research referenced in this microburst background chapter is based on data gathered in the 1978 NIMROD (Northern Illinois Meteorological Research on Down

bursts), and the 1982 JAWS (Joint Airport Weather Studies) projects. Doppler weather radar, as well as ground and airborne based MB data were gathered during each project and represent the most complete microburst studies yet attempted. The principle investigator for both projects was Dr. T. Theodore Fujita of the University of Chicago.

As extreme surface winds propagate outward from an actual downburst location, a hazardous low level wind shear (LLWS) condition can occur. If an aircraft flies thru low level a microburst, as in Fig 2.2, the encounter could be lethal. At position (1) in the figure, the aircraft first encounters a headwind from the MB outflow. This increases lift by increasing the total airflow over the wing. The pilot may then try to level off or possibly "power back" to stay on his projected glide slope. As the aircraft proceeds to positions (2) and (3), the headwind decreases and actually becomes a downdraft. At position (4) the aircraft altitude begins to drop and a strong tailwind is encountered; the performance of the plane is seriously degraded due to loss of lift. If the aircraft is close enough to the ground (position 5), it may be impossible to "power-out" of this tailwind before a crash occurs. For example, a jet transport or civil airliner aircraft will typically fly at an approach speed of approximately 70 m/s (140 kts), which is about 20 m/s (40 kts) above it's stall speed. McCarthy and Wilson, (1985) have shown that normal differential headwind to tailwind velocities range from 10 m/s to 48 m/s through a typical high plains MBs. Additionally, Fujita (1985), and Caracena, *et al.*, (1985) reported a 24 m/s microburst differential velocity associated with the crash during takeoff of Pan Am Flight 759 in New Orleans; July 1982. Also, aircraft performance studies from McCarthy and Wilson, (1985) strongly suggest that headwind to tailwind velocity differential greater than 20 m/s over a horizontal distance of $\approx$ 2 km are large enough to cause serious trouble for an aircraft close to the ground. This 20 m/s differential value was observed frequently during the JAWS experiment.

In the United States, between 1964 and 1982, microbursts were cited as contributing factors in at least 27 civil transport accidents involving over 490 fatalities and 200 injuries (National Research Council, 1983). Statistics from the National Transportation Safety Board (NTSB) show that in 1987 alone, there were 31 major aircraft accidents accounting
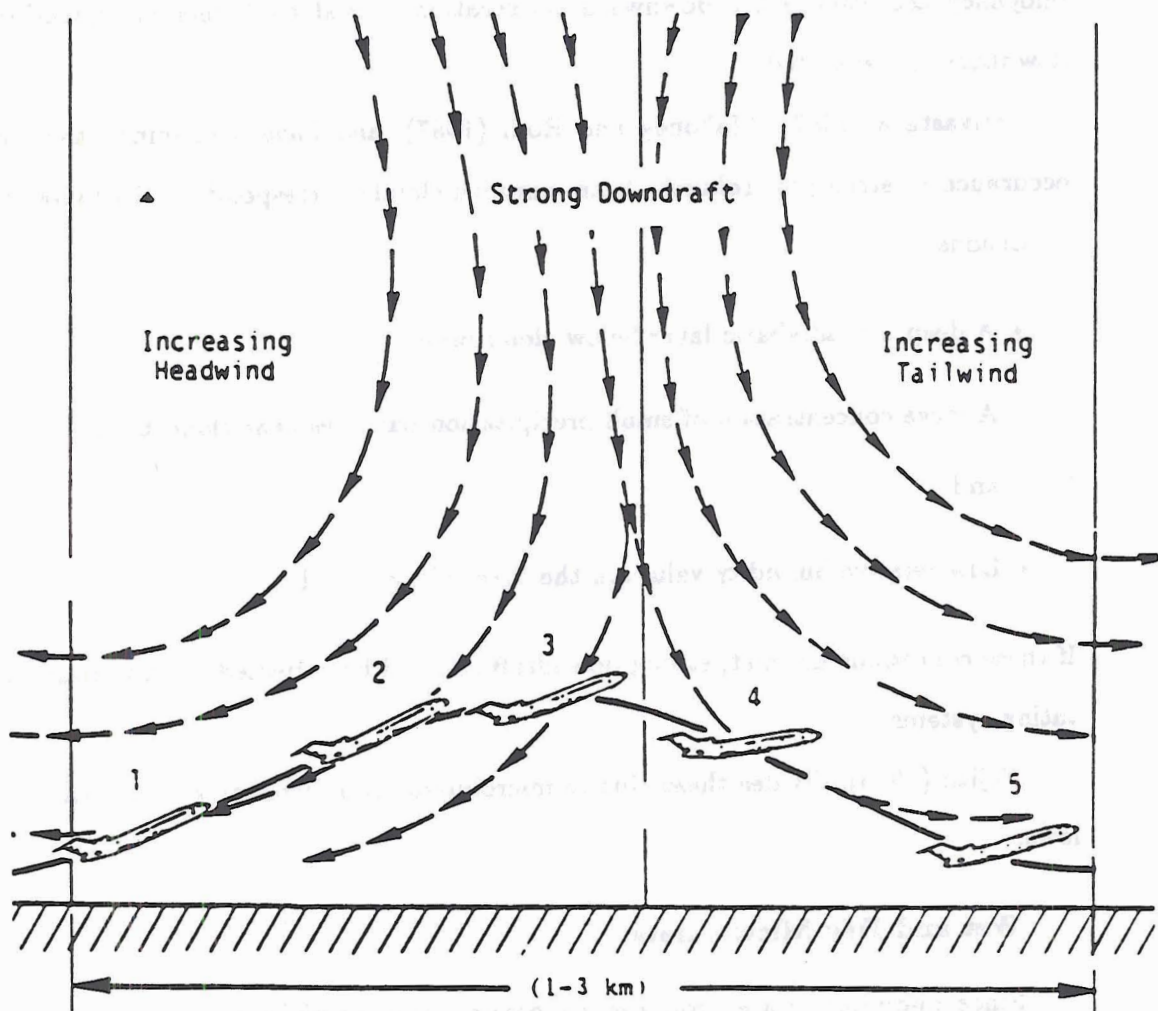
Figure 2.2: Aircraft Flight Characteristics thru a typical Microburst. A hazardous head-wind to tail-wind Low Level Wind Shear can cause the aircraft to rapidly lose altitude. From National Research Council (1983)

for 231 deaths. Many of these accidents were directly related to LLWS encountered during aircraft takeoffs and landings.

2.1 Microburst Generation and Classification

Mahoney and Rodi, 1987; Fujita, 1985; and Rodi, *et al.*, 1986 conclude that sub-cloud evaporation and melting below cloud base is most likely the predominate microburst driving mechanism. As precipitation melts or evaporates below cloud base, a negatively buoyancy accentuates the downward acceleration caused by falling precipitation and a downburst is generated.

Srivastava (1987), Mahoney and Rodi (1987), and have determined that probable occurance of strong microbursts from cumulus clouds correspond to the following three conditions:

- A deep dry adiabatic layer below cloud base.

- A large concentration of small precipitation particles near cloud base.

  and

- Low relative humidity values in the descending parcel.

If these conditions are met, strong downdrafts should be expected in and around precipitating systems.

Fujita (1985), divides these elusive microbursts into distinctive subcategories as follows:

Wet and Dry Microbursts

Since microbursts are produced by precipitation particles as they fall through the atmosphere, it is convenient to classify them as either wet or dry. For our purposes we can define a "wet" MB as a small downburst event where precipitation reaches the ground during the maximum divergent surface wind period of the microburst. However, in dryer regions of the U.S. a downburst may initiate at a relatively high cloud base altitude and the precipitation particles may completely evaporate before they hit the ground. The

downward momentum and negative buoyancy produced within this rainshaft can still accelerate these winds to the surface to produce a "dry" microburst. This difference is illustrated in Figure 2.3. These characteristics manifest themselves by prevailing humidity values. In NIMROD data (Chicago, Il), 36% of the studied microbursts were dry. In contrast, 83% of the JAWS (Denver, Co) microbursts were dry.
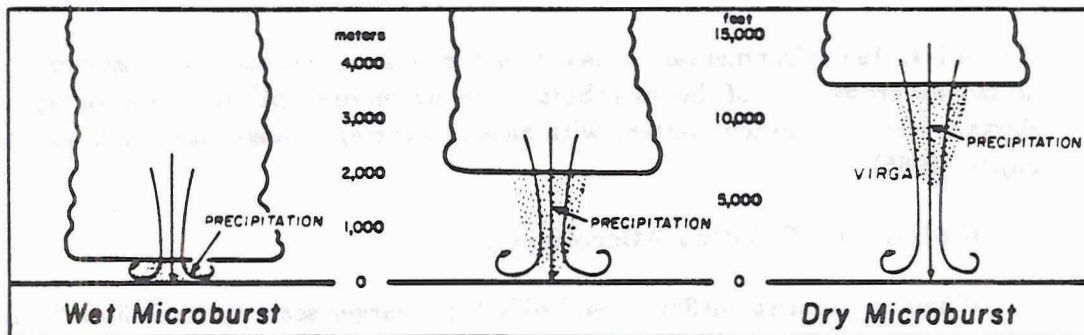
Figure 2.3: Wet microbursts occur most frequently in the more humid parts of the world. Dry microbursts are more frequent in dryer areas with high bases of convective clouds. from Fujita (1985)

Stationary and Traveling Microbursts

A stationary MB spreads radially outward inside an undisturbed environment. The outflow winds are therefore symmetric about any horizontal axis. Since most MBs are imbedded in some form of ambient air flow, this circular outflow distorts into a more elliptical pattern. In this case the front side wind intensifies and the backside wind weakens creating a crescent shaped area of high winds (Fig. 2.4).

A fast-moving MB is characterized by the more parallel streamlines shown in figure 2.4. Dr. Fujita was able to classify these MBs by comparing the strength and direction of environmental winds to the surface damage patterns found from many mid-western MB studies.
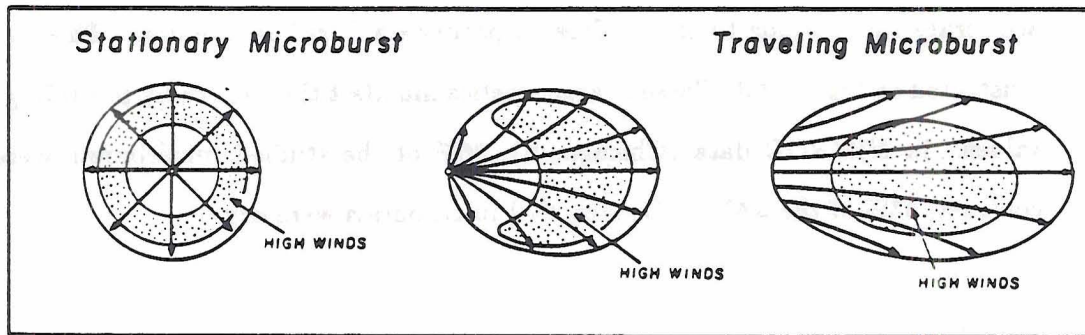
Figure 2.4: As environmental winds increase from zero to some given static magnitude, the horizontal crossection of the microburst becomes more elliptical. A stationary microburst shows a starburst airflow pattern with an annular ring of associated high winds. From Fujita (1985)

Radial and Twisting Microbursts

When microburst outflow is embedded in a larger scale cyclonic flow "twisted" outflow streamlines may result. This is a special category of the traveling MB where the environmental flow is not straight (Fig. 2.5). These often occur within mesocyclones.
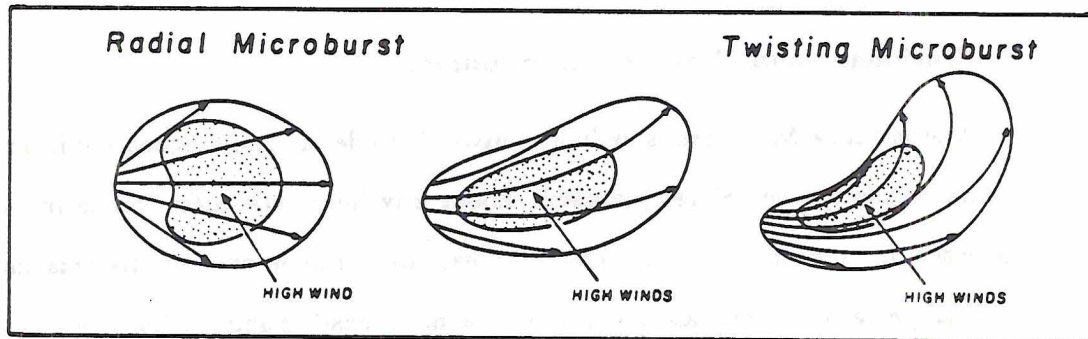
Figure 2.5: Radial and Twisting Microbursts. Environmental winds may not be straight, but may be curved. Such could be the case if the downburst winds were embedded within some larger scale cyclonic flow. From Fujita (1985)

Midair and Surface Microbursts

Wilson, *et al.*,(1984) have shown that not all microbursts descend completely to the ground. If a MB shows it's characteristic divergent flow above a typical anemometer

height, it is classified as a mid-air MB. Figure 2.6 illustrates the lifecycle of a descending microburst. A mid-air MB may or may not reach the ground. If it does, outburst winds
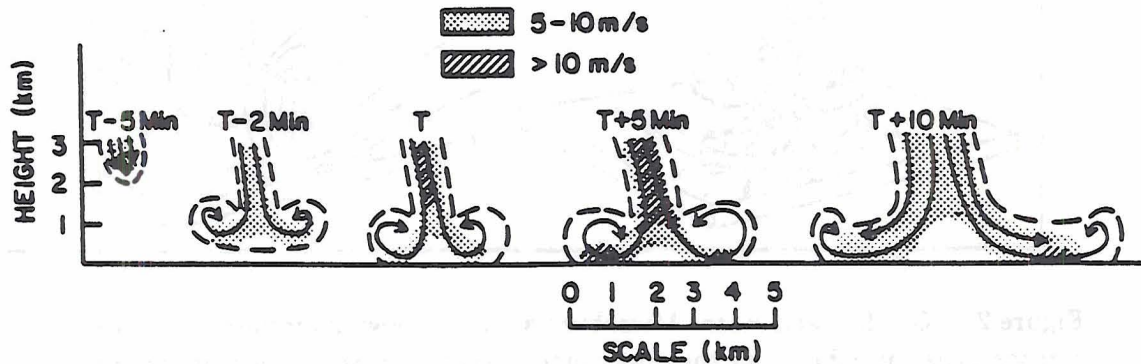
Figure 2.6: A vertical cross section of the evolution of a microburst wind field based on Doppler observed wind velocities in the JAWS experiment. T is the initial time of divergence at the surface and the shading denotes the vector wind speeds. From Wilson, *et al.*, (1984)

develop immediately upon touchdown; then the event is classified as a surface MB.

Outflow and Rotor Microbursts

An outflow microburst is the surface manifestation of the MB downflow as it encounters the ground. Outflow microbursts are often encircled by a vortex ring (Figure 2.7), and are the most common type of microburst.

This ring vortex continues to stretch as the outflow pattern increases and the MB matures. After a "stretching limit" is reached, the horizontal vortex is cut into several pieces or roll vorticies, each with it's own horizontal axis. These rolls can move away from the source area and cause locally gusty winds lasting two to three minutes; these are rotor microbursts.
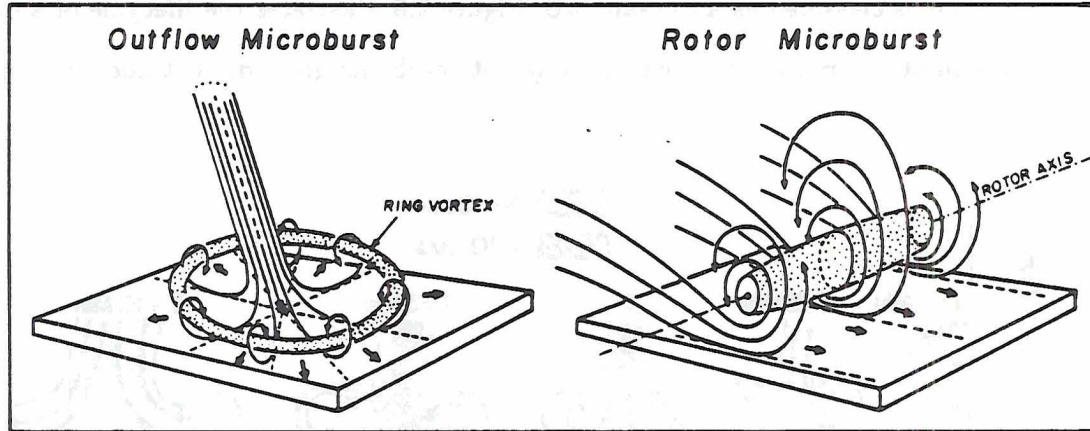
Figure 2.7: Outflow and Rotor Microbursts. An outflow microburst can often expand into a rotor type microburst as the ring vortex breaks up as the microburst matures. Some rotor microbursts develops from larger scale macrobursts and gust fronts.   From Fujita (1985)

2.2 Methods of Microburst Detection

2.2.1 Ground Based Sensing Systems

Low-Level Wind Shear Alert System

After several airline crashes during the mid-70's, the Federal Aviation Administration (FAA) developed the Low-Level Wind Shear Alert System (LLWSAS) (Goff, 1980), and (National Research Council, 1983). This system typically consists of an array of ground based wind velocity measuring instruments, located at or near an airport. Figure 8 depicts the original LLWSAS anemometer network.

The system consists of a centerfield wind sensor and 5 outlying sensors normally located about 2 miles from the center site. More modern systems may have more anemometers in the array, providing better spatial resolution for microburst detection. For instance, at Stapleton Airport near Denver, CO the LLWSAS has a total of 12 sensors.

These propeller vaned sensors rise from 10 to 60 feet above the ground as necessary to obtain unobstructed air flow above the local terrain. In order to place and design the most effective LLWSAS, local weather factors are also considered. Each site is sampled

BOUNDARY
SITE

7.5 S RC
LOWPASS
ELECTRONIC
FILTER

3 km
SPACING

RADIO
LINK

CENTRAL
MINIPROCESSOR

CENTERFIELD
SITE

BOUNDARY SITE
SCAN RATE 7-10 S (~11 S)
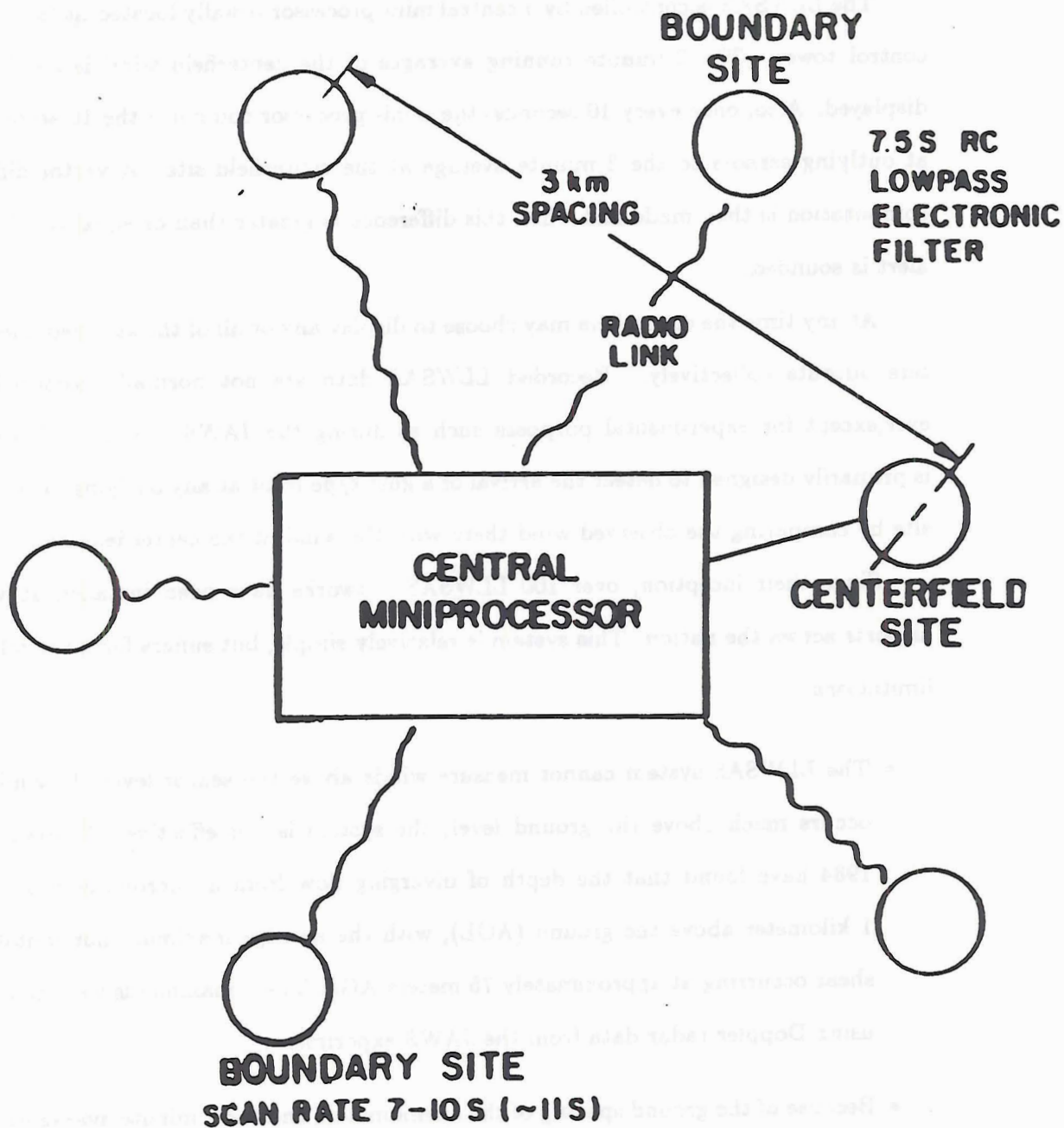
Figure 2.8: The Low Level Wind Shear Alert System configuration as originally conceived by the Federal Aviation Administration.   From Bedard, *et al.*, (1984)

every 10 seconds and the centerfield site is considered a reference site where a 2 minute running average of wind velocity is maintained.

The LLWSAS is controlled by a central mini-processor usually located at the airport's control tower. The 2 minute running averages of the centerfield wind is continuously displayed. Also, once every 10 seconds, the mini-processor compares the 10 second wind at outlying sensors to the 2 minute average at the centerfield site. A vector difference computation is then made and when this difference is greater than or equal to 15 kts, an alert is sounded.

At any time the controllers may choose to display any or all of the sectored anemometers outputs collectively. Recorded LLWSAS data are not normally recorded however,except for experimental purposes such as during the JAWS project. This system is primarily designed to detect the arrival of a gust type front at any outlying anemometer site by comparing the observed wind there with the wind at the centerfield site.

Since their inception, over 100 LLWSAS networks have been installed at various airports across the nation. This system is relatively simple, but suffers form the following limitations:

- The LLWSAS system cannot measure winds above the sensor level. If wind shear occurs much above the ground level, the system is not effective. Wilson, *et al.*, 1984 have found that the depth of diverging flow from a microburst is less than 1 kilometer above the ground (AGL), with the average maximum horizontal wind shear occurring at approximately 75 meters AGL. These maximums were calculated using Doppler radar data from the JAWS experiment.

- Because of the ground spacing of the anemometers and the 2 minute averaging of the centerfield station, time and spatial resolution is poor. As the distance between the centerfield sensor and any remote sensor can be as much as 2 kilometers, effective wind shear resolution could be too small when dealing with microbursts. Also, any brief wind shear occurrence spanned by a microburst may not be detected at the centerfield site due to the 2 minute averaging technique.

• Any surface wind shear events detected are not necessarily the winds along a flight path. This just means that if the runway and flight path are not confined within the LLWSAS area, positive wind shear identification cannot be made.

It is clear form the JAWS project results that increasing the LLWSAS sensor density and improving general system responsiveness would greatly enhance the systems ability to detect microbursts near the earth's surface. However, this would only address one of the limitations mentioned above and still falls short in providing explicit wind shear information along a flight path and at altitudes greater than near surface.

Pressure Sensors

At Dulles International Airport outside Washington,D.C., a network of groundbased anemometers was coupled with an array of microbarographs to try and detect low altitude wind shear from microburst activity. Bedard,*et al.*, (1979), found that microbarographs used in conjunction with a LLWSAS could give lead times of shear producing outflow winds as much as 3 minutes ahead of anemometers alone. However, a 3-month test at the Hartsfield International Airport in Atlanta showed that some microbursts could impact the ground between the microbarographs and never be picked up as a pressure change. The study implied that the number of barographs required coupled with an effective array size would make the system impractical to maintain and operate. Except for inferring some vertical air movements well above ground level, this system has the same drawbacks as the LLWSAS, and is much more complex due to the addition of the barographs.

Conventional Radar

Since most conventional weather radars are designed to detect precipitation sized particles, one can only infer the presence of hazardous outflow winds from a precipitating system. Every pilot knows to stay well away from visually observed thunderstorms. However, Fujita and Wakimoto, (1983) were able to determine that not all downburst events are "wet" . They found that in the JAWS project 155 out of 186 recorded microbursts were "dry"; no rain reached the ground. This ratio will change based on the available

moisture in the atmosphere as illustrated in NIMROD project data where only 18 of 50 studied microbursts were dry. As a result, conventional radars are not capable of detecting all microbursts. The absence of a radar echo over an airport does not mean that wind shear does not exist.

Terminal Doppler Weather Radar

A current method of MB detection at many U.S. airports involves the use of a narrow Terminal Doppler Weather Radar (TDWR). A Doppler system directly measures the velocity of microburst winds, or more accurately, it measures the component of the atmospheric scatterers' motion towards or away from the radar. Since the radar can only detect motion along a path coincident to the actual radar beam, any cross-beam winds cannot be directly measured by a single Doppler system. When a micorburst is symmetric in horizontal cross- section the single Doppler derived wind pattern of a downburst can be recognized. Unfortunately, microbursts are frequently imbedded in some form of larger scale airflow that creates an asymmetric flow pattern with an associated asymmetric outflow of shear producing winds. (Figure 2.9)

To solve this problem, multiple Doppler radars can be used. If the same volume of atmosphere is examined from two (or more) different locations, an accurate picture of the wind field results. Figure 2.9 illustrates the horizontal and vertical structure of a JAWS reported microburst from a dual Doppler configuration. These multiple systems are not only accurate in locating most mature microbursts but used together they have more time to completely scan the atmosphere at considerable distance above the ground where microburst precursors can be detected. This capability can increase advance warning time for pilots in local flight patterns.

Evaluation of these TDWRs at many U.S. airports is now in progress, (McCarthy and Wilson, 1986, Turnbull,et al., 1989; Campbell, et al., 1989). At present, these radar systems have several deficiencies that affect their ability to meet effective mictoburst detection and warning criteria.

- As the radar needs to scan close to the horizon where ground clutter is a problem, a TDWR system cannot directly measure winds in the lowest 50-60 meters of the
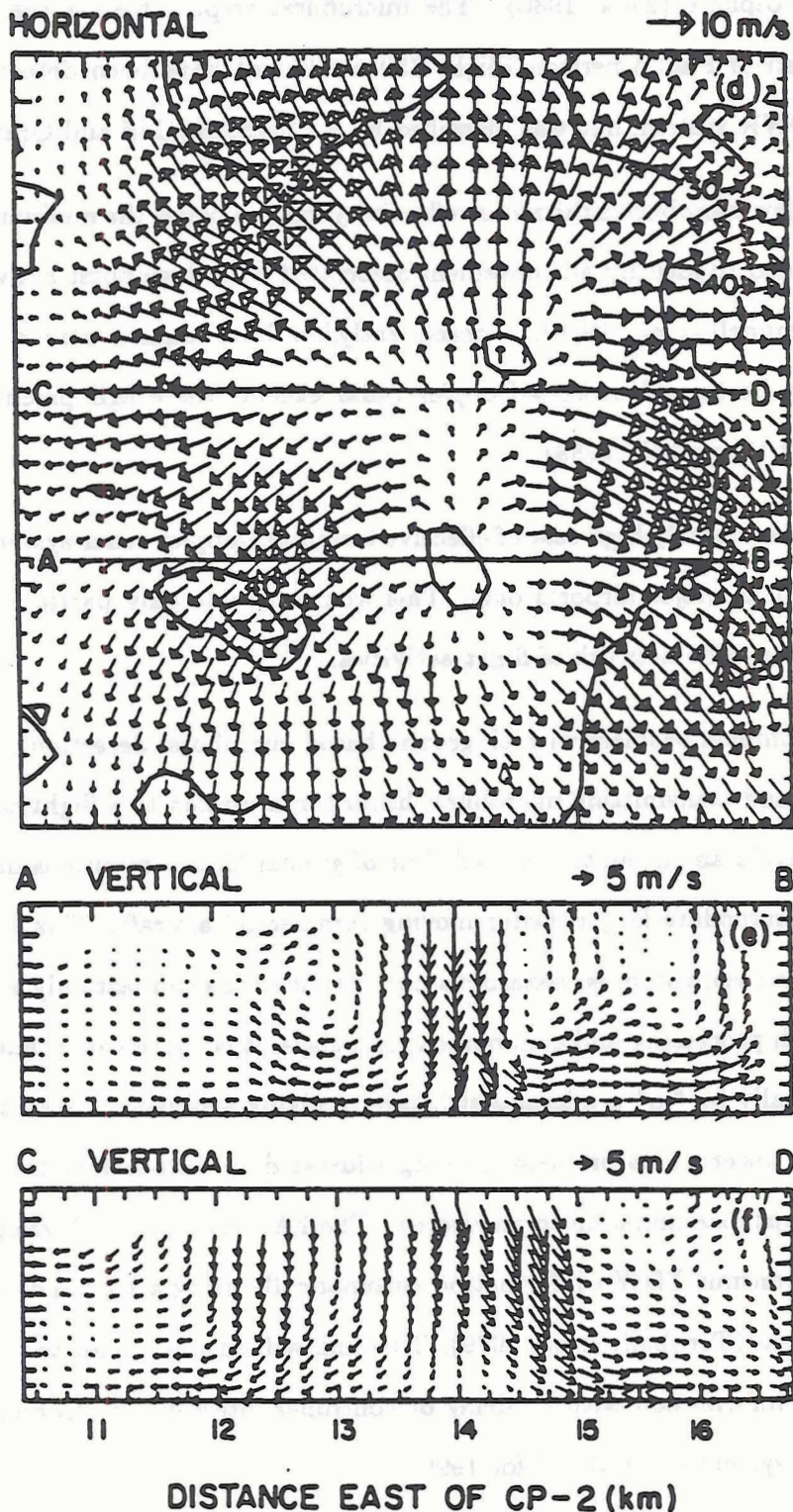
Figure 2.9: The symmetric nature of this microburst would allow analysis by a single Doppler radar system although these vector winds were determined by a dual system. This is a JAWS reported microburst from 14 July 82 where contours are radar reflectivity factors (dBZ_e).　　From Wilson and Roberts (1983)

atmosphere (Eilts, 1986). The microburst responsible for the 1982 New Orleans crash of Pan American Flight 759 would not have been detected by the planned TDWR system, but was identified by a LLWSAS (Goff and Gramzow, 1989).

- In dry microbursts the radar reflectivity may be below the minimum detectable signal needed to identify air movement associated with downburst activity (Smythe, 1989; Campbell,*et al.*, 1989). Consequently,low level manifestations of dry microbursts may be missed using a Doppler radar except where MB precursors are identified aloft (Campbell, 1989).

- The extremely high cost of effective terminal Doppler radar systems will allow place-ment at major airports only. This would provide only partial coverage for a busy nation-wide network of flight activities.

- A common problem with all ground based microburst detection systems is in analyz-ing and transmitting microburst hazard information to a flight crew in enough time to avoid an encounter. A lead time of greater than 1 minute is desirable in order to accommodate larger, faster moving commercial aircraft. This is difficult as, under some circumstances, hazardous microburst winds can last only a couple of minutes. With processing and communication delays, it is conceivable that an airplane could actually be "in" a microburst before receiving avoidance instructions from the con-trol tower. This problem is being addressed by automating the TDWR algorithm output dissemination to an aircrew. The FAA is currently developing the capability to transmit TDWR information automatically using a special data link transponder system (Turnbull, *et al.*, 1989). This link will enable a pilot to get displayed, direct MB information with no delay or controller interception. Complete deployment of this system is scheduled for 1996.

Nexrad

NEXRAD, or NEXt generation RADar, is an advanced pulsed Doppler Radar that is chiefly designed to track such weather events as severe storms, tornadoes, tropical cyclones,

hail, severe turbulence, and high wind shears. These new systems are scheduled for installation at various locations throughout the U.S. during the 1990's. Each of these NEXRAD installations will analyze local weather at ranges exceeding 200 miles and heights of 60,000 feet at a rate of once every 3.5 minutes. Due to this large sampling volume each NEXRAD unit must rely on an extreme amount of automation in order to effectively process this vast amount of data.

Because the scan rate is so slow it is doubtful that a non-dedicated NEXRAD could be effective in the timely detection of microbursts. Also, the height of the NEXRAD radar tower and the requirement of an unobstructed view of approximately 200 miles would limit a NEXRAD's system's useability around many airports.

The NEXRAD radar can out perform and suppress ground clutter better than conventional radars and a stand alone system could be of benefit near an airport if it were customized to an appropriate scan rate ideal for detecting microbursts (approximately 30 sec/scan). However, cost is again a limiting factor. Coupled with this problem, NEXRAD uses a 2700-2900 MHz frequency band which is used by many other radar systems across the U.S.; interference could result. For these reasons it would seem impractical to expect extensive NEXRAD coverage of nationwide airports.

FM-CW Radar

A Frequency Modulated - Continuous Wave Doppler Radar could be used instead of pulsed Doppler radar for microburst detection. This style of radar has many of the same characteristics as does a pulsed Doppler unit. A key difference between the two is that a pulsed Doppler transmits high-power using low duty- cycle pulses where an FM-CW unit transmits a low-power, full (constant) duty cycle signal that is frequency modulated. This enables the the radar to use a high average power over a broad signal bandwidth producing high sensitivity and resolution at very short ranges. Additionally, high resolution diminishes the ground clutter effect.

This radar and it's application to the microburst detection problem may provide a usable system; more research is needed.

Doppler Lidar

An appropriately designed Lidar system can measure winds in optically clear air by detection the backscattered power from small atmospheric particles. This system works on the same principles as that of Doppler radar but using light frequencies. Lidar has an advantage over radar as the narrow beam is free of ground clutter effects. A distinct disadvantage over the radar system is that the Lidar beam can be heavily absorbed by rain, clouds, and fog over ranges in excess of 1 mile. This method should be investigated further, as it could prove very useful in microburst detection. Past research indicates, however, that size, weight, power requirements, and range deficiencies must be overcom before the LIDAR system can be a serious contender for airborne MB detection.

Aircraft (Reactive) Inertial Systems

When an aircraft enters a wind shear/turbulent environment it can experience large momentum changes in any direction. An aircraft equipped withan inertial navigation reactive system (INS)[1] can sense and compute parameters such as critical pitch angles, relative wind, ground speed and vertical motion and display them to the pilot. Some elaborate reactive systems can automatically make needed "in-flight" adjustments in order to correct for more serious momentum changes.

Even though these systems can be extremely sophisticated, they are not able to provide the advanced warning time necessary to avoid a MB encounter. These a reactive systems only identify LLWS when the aircraft is actually experiencing a wind shear event. Since avoidance of a MB is the only guarantee that associated LLWS will not become a flight hazard, the reactive system is not a viable alert system.

2.2.2 Airborne Remote Sensing of Windshear

For many years aviators have known that heavy rain shafts associated with thundershowers can conceal hazardous storm outflow winds. But Fujita's studies have shown

---

[1]Designed and built by such companies as: Safeflight Instrument Corp., Sperry Corp, Sundstrand, Flight Dynamics, and Honeywell Inc.

that even benign looking rain clouds can generate dangerous microbursts. Small, harmless looking convective clouds will spawn microbursts even where precipitation does not reach the ground. It is this fact that sometimes makes visual microburst detection almost impossible. Because of their dangerous nature, the Federal Aviation Administration (Federal Registry, 1988) now recognizes the need for an airborne low level wind shear alert system that will:

- supplement the present and planned deployments of LLWSAS and warning systems, and

- provide "on-board" detection of LLWS enabling commercial aircraft to avoid hazardous MB conditions, especially during the critical landing and takeoff phases.

Timely and accurate detection of wind shear activity from an aircraft provides an ideal flight safety position. All the groundbased systems previously mentioned can identify microbursts under specific and sometimes exclusive weather conditions. What is needed however, is a sensing system mounted on an aircraft that scans straight ahead in the flight path and alerts the pilot immediately of any upcoming hazardous LLWS. An effective on-board system would provide microburst detection wherever and whenever it is required by the pilot. Cost and maintainance should be low. Above all, LLWS information would be immediately available to the flight crews without having to go thru the tower controllers first, or wait for direct transmission of an actual surface observation.

The following systems have some promise in this application and will be briefly discussed. Special emphasis is placed on the passive infrared radiometry method devised by Kuhn,*et al.*,1983 and Sinclair and Kuhn (1990), and forms the nucleus of Chapter 2.

Microwave Doppler Radar

Any radar mounted on an airplane must be able to detect upcoming windshear without severe side-lobe effects. Some airborne Doppler radars currently in use (NOAA and NASA) offer similar capabilities to that of a ground based system, but these units are

mounted on aircraft where space and power requirements are not a problem. Doppler radars currently available for airborne commercial use appear to be small (under powered), insufficiently sensitive, and provide inadequate spatial resolution to define a LLWS event (National Research Council, 1983). Further development of this radar application is required for commercial use.

Doppler Lidar

Forward looking LIDAR may have some future success in windshear detection, but current systems are focused to measure the winds at ranges of approximately 1 mile ahead of the aircraft. This is due to serious attenuation problems with the visible and near visible wavelengths used for LIDAR. These systems can be rugged and reliable, but with the above range limitations, an adequate avoidance time is impossible to attain.

Chapter 3

THE MICROBURST SCENARIO

This chapter will emphasize a technique for actual microburst detection using an infrared radiometric technique similar to one developed by Kuhn, *et al.*, (1983). Kuhn's method is based on the temperature difference measured near the aircraft and the MB temperature deduced from the remote radiometric measurements. Our technique utilizes the temperature difference between two atmospheric paths, one path containing the MB and a second path close to but outside the MB containing only the ambient environment. This differencing technique provides system noise suppression and hence lower measurement thresholds and data clarity. Additionally, we will discuss a ranging technique using horizontal weighting functions (Kuhn, *et al.*, 1983). Previously discussed characteristics of dry microbursts will be used.

3.1 A Simple Microburst Model for Infrared Detection

Except for the ground-based pressure sensing method mentioned in Chapter 2, all current techniques for detecting microbursts attempt to measure MB winds either directly or indirectly. The proposed Forward Looking Infrared Radiometer system (FLIR) will detect the microburst based on it's downburst temperature difference as compared to the environmental temperature.

Fawbush and Miller (1954), Foster (1958) and Proctor (1989), have shown a clear relationship between a downburst's temperature and the ambient atmospheric temperature (ΔT). Figure 3.1 illustrates these findings and shows that a colder MB will generate larger surface gusts. This is, at least, intuitively pleasing as a more negatively buoyant or colder air mass should have a larger amount of associated kinetic energy.
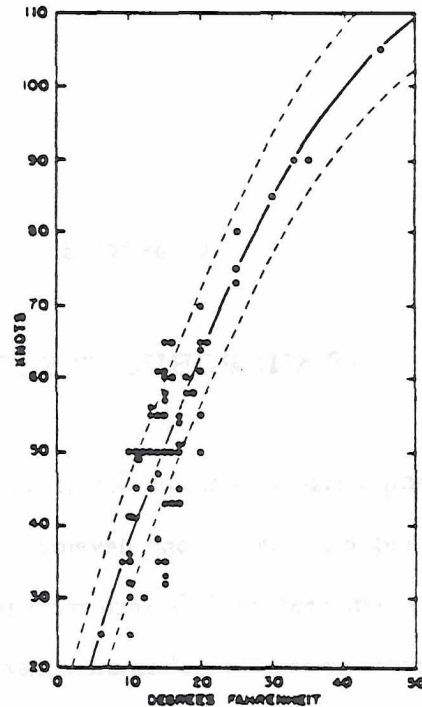
Figure 3.1: Peak gusts and temperature differences in thunderstorms showing the regression curve and standard error of estimate curves. The abscissa is temperature just prior to a thunderstorm occurance minus the temperature immediately after the downrush of air. From Fawbush and Miller (1954)

Fujita, (1985), Fujita (1986), and Sinclair and Kuhn (1990) have determined that potentially hazardous downbursts can have absolute temperature differences ranging from ≈ 2.0 to greater than 15 deg C as compared to the surrounding atmospheric temperature. Within this range of temperature difference, headwind to tailwind differentials frequently reach our previously established 20 m/s safety threshold and become a low level wind shear hazard when encounter by a low flying aircraft. Keeping this in mind, our radiometer must be able to scan the atmosphere ahead and detect a microburst shaft that may only be a couple degrees C different than that of the environment ($\Delta T = 2^\circ$ C).

In this study, we define ΔT as the temperature difference between the microburst downdraft shaft and the ambient environment. This is not to be confused with the divergent portion of the downburst outflow. Statistical results from Fujita, (1985) reveal that approximately 40% of the JAWS and NIMROD microburst outflows are warmer than their environment. These warm outflow winds have been influenced by the mixing of extremely warm surface layer air, and therefor may not truly be representative of the actual microburst shaft temperature.

The following assumptions are made for our analysis and model study:

1. The microburst is embedded in an isothermal atmosphere where the only temperature variation along the pathlength is from the ΔT of the MB.

2. Pressure along the pathlength is assumed to be constant. Fujita (1985) recorded pressure changes of no more than 6 mb associated with the occurance of a microburst. With an ambient pressure of 950 mb, a 6 mb pressure differential amounts to less than a 1% total pressure change and is neglected in our radiance calculations.

3. Atmospheric constituents that absorb/emit IR radiation are limited to CO_2 and atmospheric water vapor (Chapter 4). Aerosols have been omitted due to their small effect on atmospheric transmission in our wavelength region of interest. The LOWTRAN7 code (see appendix) has shown that aerosol contribution to total atmospheric absorption in a typical mid-latitude summer atmosphere is less than 0.2%. This is a broad assumption and may not hold true in localized areas of heavy pollution. Also, coastal areas may contain large concentrations of sea salt aerosols which could significantly degrade total atmospheric transmittance.

   particle

4. The beam volume of our theoretical instrument is completely filled with absorbers in conditions of local thermodynamic equilibrium.

5. Figure 3.2 depicts the model atmosphere used to calculate the radiance received from a hypothetical MB in an aircraft flight path during landing. This proposed FLIR system will employ an infrared radiometer to scan the flight path ahead of the aircraft. As shown in Figure 3.2 the scanning scheme will be horizontal as well as vertical and commence during the final approach stages of a landing aircraft. An aircraft preparing to take-off will need to elevate the radiometer a few degrees in order to avoid any thermal changes in the ambient atmosphere caused by the MB outflow at or near the surface. This small angle elevation would essentially aim the pencil beamwidth of our radiometer at an above ground level (AGL) of greater than

25

300 meters to avoid this possible MB outflow contamination region. For this study, we will make measurements of the MB as seen by the landing aircraft only; due to the more straight forward geometry.

6. Using Fujita's definition, the MBs in our model will be "dry". However, we will perform radiance calculations using a variable concentration of water vapor within the MB. This will allow us to determine the radiative influences of water vapor fluctuations within the MB, versus the modeled radiance received. We will assume there are no water droplets in the scanned downshaft volume.

Also, since normal glide slope altitudes are below cloud base, no cloudy atmospheres are incorporated in the modeled scans. Drastic absorption by clouds would prohibit the proposed IR technique.

Using the 12.5 to 15μm portion of the electromagnetic spectrum, the radiometer will scan ahead and measure atmospheric radiance. Once focused on a possible MB shaft, the radiometer begins to scan a horizontal azmuithal sector ahead of the aircraft. During this scan a radiance measurement of the ambient atmosphere is taken. In a isothermal atmosphere, the radiometer will naturally receive the same radiance from all parts of scan. However, when a cold microburst is encountered, the thermal difference is detected as a drop in radiance. If this calculated difference in received radiance (ΔN) meets or exceeds some pre-determined threshold value, a low level wind shear alert is sounded in the cockpit as the presence of a microburst is inferred.

In addition, low level penetration studies of microbursts shafts by Kuhn, *etal.* (1983), Kuhn and Sinclair (1987) and Sinclair and Kuhn (1990) have shown that the magnitude of the time rate of change of temperature difference ($\frac{\Delta T}{\Delta t}$) can also be used for MB identification. Their findings suggest that an observed gradient of -0.5$^\circ C$/s is sufficient to prompt a warning for low level wind shear. So,if this low level negative rate threshold is sensed during the instrument scanning process, a wind shear alert would follow.

Our radiometric is also designed to determine the range of an encountered microburst. A ranging capability is necessary in order to provide adequate avoidance time at expected
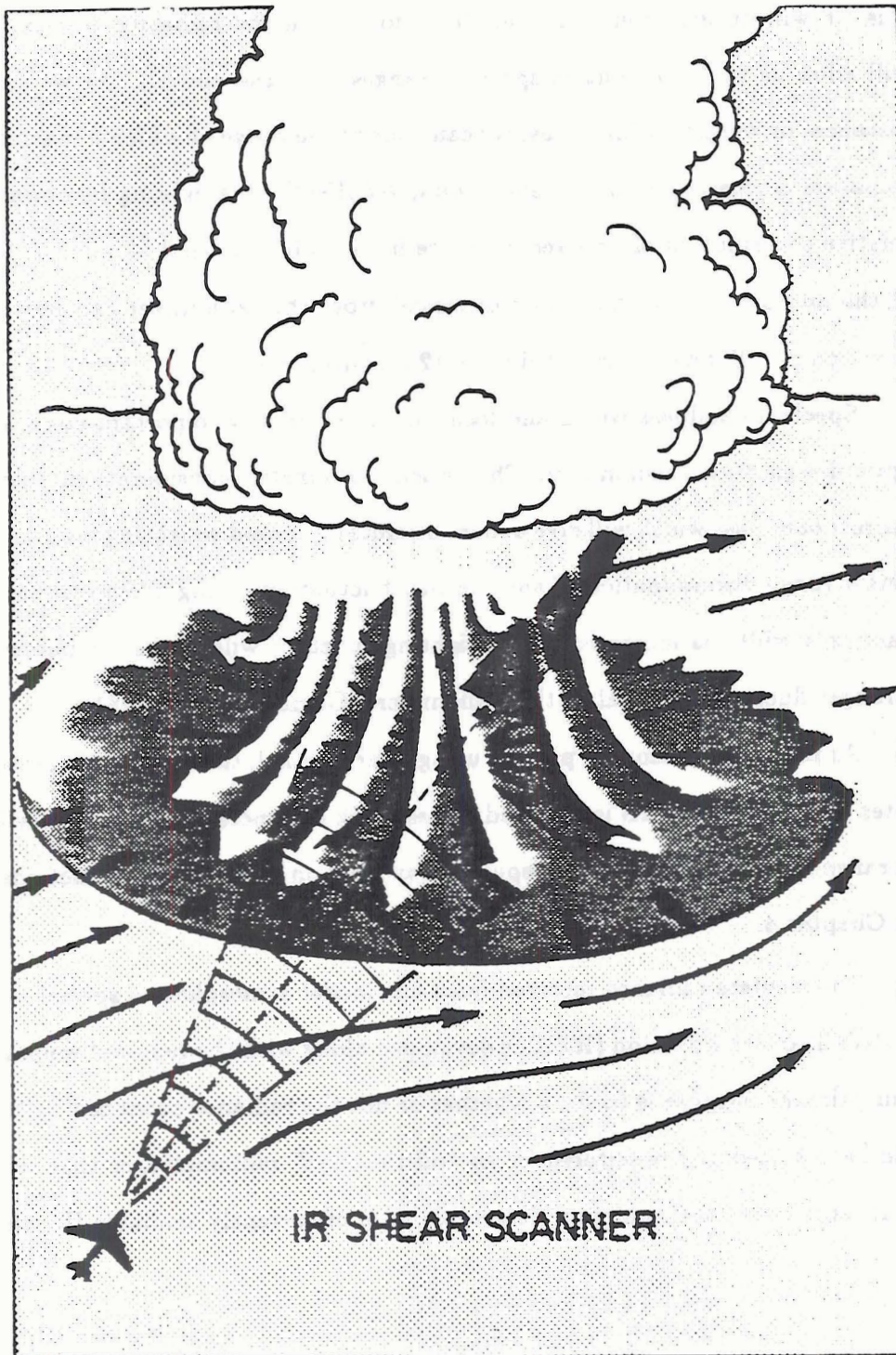
Figure 3.2: The FLIR system will scan the aircraft flightpath to detect the change in temperature (ΔT) between the environmental air and that of the microburst. This figure illustrates an azimuthal scan across the flight path at one pre-determined range from the aircraft.

flight speeds, and to track the microburst as it moves through the flight path. To do this we will develop weighting functions for use in the radiative transfer equation that will allow us to "look" out at specified ranges from the aircraft. As we vary the "look " distances or weighting functions, we can change the range at which a maximum amount of radiation is received at the sensor (Kuhn,*etal.*,1983). A weighting function represents the relative contribution of received radiance in our infrared band at various distances ahead of the aircraft. Thus, the " look distance" from the radiometer can be adjusted by the selection of different filters within our 12.5 to 15 μ range.

Spectral bandpass width and location are extremely important considerations in the optic design of our radiometer. Theoretical radiometric considerations show that a more narrow bandpass width will give a more discrete or peaked weighting function and therefore better range discrimination of any thermal fluctuations along our horizontal path. As the bandpass width is increased, the weighting function will be flatter but will receive the stronger fluctuation signal at the radiometer, (Caracena, *etal.*, 1981).

As part of the scanning process using a far channel, the radiometer sensor will initiate filter changes once a MB is detected. These look distances/filter changes will allow a scan in range from the aircraft. Atmospheric transmission and weighting functions are discussed in Chapter 4.

To calculate radiance received from our model atmosphere a special form of the Radiative Transfer Equation (RTE) is developed along with the required weighting functions. Our primary purpose is to show whether or not the radiance produced by this microburst can be detected and monitored by an "off-the-shelf" radiometer, or that this input signal is at least above the minimum detectable level of currently available IR sensors.

Chapter 4

THE RADIATIVE TRANSFER EQUATION

This chapter presents a concise derivation of the radiative transfer equation. A basic description of atmospheric transmittance as required for use in our horizontal application of the radiative transfer equation is also discussed. We will focus our atmospheric transmission study along the near wing of the 15μ CO_2 absorption band. A basic form of Schwartzchild's equation for use in this part of the spectrum is given and can be explicitly used to calculate the radiance received from the atmospheric MB scenario developed in Chapter 3.
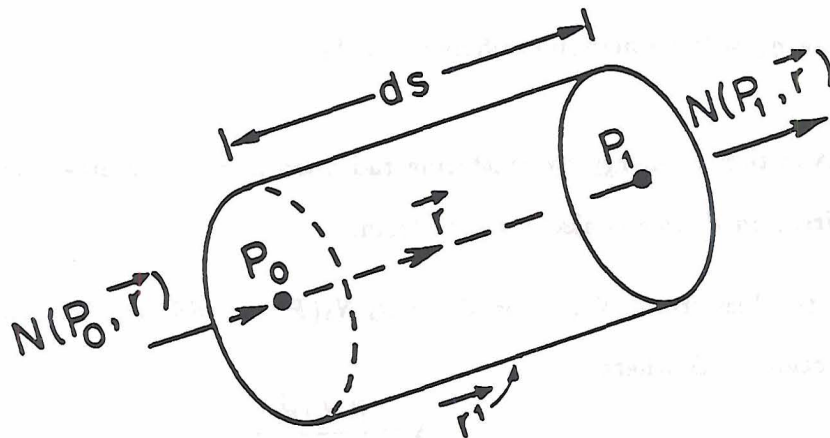
$$N_{(P_1,\vec{r})} = N_{(P_0,\vec{r})} + \frac{\partial N}{\partial S}\,dS \qquad (4.1)$$

where $N_{(P_0,\vec{r})}$ is spectral radiance at point P_0, traveling in the direction $\vec{r}$, and $N_{(P_1,\vec{r})}$ is the spectral radiance emerging from the volume in the path $\vec{r}$.

We now define four possible effects on the partial derivative term in equation (4.1):

Term A $\rightarrow$ Extinction by absorption between P_0 and P_1; this acts as a depletion term.

$$A = -\kappa_\lambda\, N_\lambda(P_0, \vec{r})\, \rho_{gas}\, dS,$$

where κ_λ = the absorption coefficient, and ρ_{gas} is the density of the absorbing gas considered. In the following derivation, we will omit the "gas" subscript for ease of notation.

Term B $\rightarrow$ Extinction by scattering between P_0 and P_1; this is also a depletion term.

$$B = -\sigma_\lambda\, N_\lambda(P_0, \vec{r})\, \rho\, dS,$$

where σ_λ = the scattering coefficient.

Term C $\rightarrow$ Emission from within the cylinder; a source term.

$$C = \eta_\lambda\, \rho\, dS,$$

where η_λ = the emission coefficient (m^{-1}).

Term D $\rightarrow$ Addition of energy by scattering radiation from other directions, or into $\vec{r}$ from a direction $\vec{r^j}$; this is also a source term.

Let the loss from $N_\lambda(\vec{r^j})$ be $\Gamma = \sigma_\lambda\, N_\lambda(P_0', \vec{r^j})\, \rho\, dS$ and let the gain into the $\vec{r}$ direction be Δ, where

$$\Delta = \frac{\Gamma\, P_\lambda(\vec{r^j}, \vec{r})}{4\pi},$$

and

$$\frac{P_\lambda(\vec{r^j}, \vec{r})}{4\pi}$$

is the scattering phase function.

Substitute Γ into the above equation.

$$\Delta = \sigma_\lambda N_\lambda(P_0', \vec{r})\, \frac{P_\lambda(\vec{r^j}, \vec{r})}{4\pi}\, \rho\, dS \tag{4.2}$$

We integrate equation (4.2) over all directions $\vec{r'}$, or over the entire solid angle to get;

$$D = \frac{\sigma_\lambda}{4\pi} \int_{r'} N_\lambda(P_0', \vec{r}) \, P_\lambda(\vec{r'}, \vec{r}) d\vec{r'} \, \rho \, dS$$

We combine these four terms with the first term in (4.1) where $\partial N / \partial S = A+B+C+D$ or;

$$N_\lambda(P_1, \vec{r}) = N_\lambda(P_0, \vec{r}) - \kappa_\lambda \, N_\lambda(P_0, \vec{r}) \, \rho \, dS - \sigma_\lambda N_\lambda(P_0, \vec{r}) \, \rho \, dS +$$

$$\eta_\lambda \, \rho \, dS + \frac{\sigma_\lambda}{4\pi} \int_{r'} N_\lambda(P_0', \vec{r'}) \, P_\lambda(\vec{r'}, \vec{r}) d\vec{r'} \, \rho \, dS \qquad (4.3)$$

Now, rearrange (4.3) and divide thru by $\rho \, dS$, then take the limit of the left hand side as $dS \to 0$, where,

$$\lim_{dS \to 0} \frac{N_\lambda(P_1, \vec{r}) - N_\lambda(P_0, \vec{r})}{\rho \, dS} = \frac{1}{\rho} \frac{dN_\lambda}{dS}$$

So (4.3) becomes

$$\frac{1}{\rho} \frac{dN_\lambda}{dS} = \eta_\lambda + \frac{\sigma_\lambda}{4\pi} \int_{r'} N_\lambda(P_0, \vec{r}) \, P_\lambda(\vec{r'}, \vec{r}) \, d\vec{r'} - N_\lambda(P_0, \vec{r})(\kappa_\lambda + \sigma_\lambda) \qquad (4.4)$$

From Kirchoff's Law, in local thermodynamic equilibrium conditions, the ratio of the emission and absorption coefficients is independent of the qualities of the medium and equals the spectral exitance given by Planck's Law (Chandrasekhar, 1960) or,

$$\frac{\eta_\lambda}{\kappa_\lambda} = B_\lambda$$

so,

$$\eta_\lambda = B_\lambda \, \kappa_\lambda$$

We also need to define, in our case, that $dS = \sec\theta \, dx$. Since we are looking in a single horizontal direction as nadir, $\sec\theta = 1$, so $dS = dx$. With these substitutions equation (4.4) becomes a basic form of the radiative transfer equation,

$$\frac{1}{\rho} \left[\frac{dN_\lambda}{dx} \right] = \kappa_\lambda B_\lambda - \frac{\sigma_\lambda}{4\pi} \int_{r'} N_\lambda(P_0, \vec{r}) \, P_\lambda(\vec{r'}, \vec{r}) \, d\vec{r'} - N_\lambda(P_0, \vec{r})(\kappa_\lambda + \sigma_\lambda) \qquad (4.5)$$

We can customize equation (4.5) to calculate long wave radiation transfer by ignoring all the scattering terms. This is a legitimate assumption with the absence of clouds since the radius of typical haze particles and atmospheric gas molecules are very small compared to wave lengths in the infrared spectrum (Hudson, 1969).

$$\frac{1}{\rho}\left[\frac{dN_\lambda}{dx}\right] = \kappa_\lambda B_\lambda - \kappa_\lambda N_\lambda(P_0,\vec{r}) \tag{4.6}$$

From the definition of optical depth and neglecting scattering,

$$\tau_\lambda = \int \kappa_\lambda \rho \, dz$$

so,

$$d\tau_\lambda = \kappa_\lambda \rho \sec\theta \, dz$$

or, looking in the horizontal, $d\tau_\lambda = \kappa_\lambda \rho \, dx$. If we divide (4.6) by κ_λ we can show that,

$$-\frac{dN_\lambda}{d\tau_\lambda} = B_\lambda - N_\lambda(P_0,\vec{r})$$

where the negative sign above comes from the negative relation between τ and increasing values of x. Now, multiply the above equation by $\exp^{-\tau_\lambda}$ to get,

$$-\exp^{-\tau_\lambda}\frac{dN_\lambda}{d\tau_\lambda} = \exp^{-\tau_\lambda} B_\lambda - \exp^{-\tau_\lambda} N_\lambda(P_0,\vec{r})$$

We can rearrange this to get,

$$-\exp^{-\tau_\lambda}\frac{dN_\lambda}{d\tau_\lambda} + \exp^{-\tau_\lambda} N_\lambda(P_0,\vec{r}) = \exp^{-\tau_\lambda} B_\lambda \tag{4.7}$$

Since,

$$\frac{d(-N_{(P_0,\vec{r})}\exp^{-\tau_\lambda})}{d\tau_\lambda} = -\exp^{-\tau_\lambda}\frac{dN_\lambda}{d\tau_\lambda} + \exp^{-\tau_\lambda} N_\lambda(P_0,\vec{r})$$

Equation (4.7) becomes,

$$-\frac{d(N_{(P_0,\vec{r})}\exp^{-\tau_\lambda})}{d\tau_\lambda} = \exp^{-\tau_\lambda} B_\lambda$$

or,

$$-d(N_{(P_0,\vec{r})} \exp^{-\tau_\lambda}) = B_\lambda \exp^{-\tau_\lambda} d\tau_\lambda \qquad (4.8)$$

Now, integrate in the horizontal from x_0 to x_1,

$$-N(x_0,\vec{r}) \exp^{-\tau_\lambda(z_1,z_0)} + N_\lambda(x_1,\vec{r}) = \int_{z_0}^{z_1} B_\lambda \exp^{-\tau_\lambda} d\tau_\lambda$$

which we can rearrange to get

$$N_\lambda(x_1,\vec{r}) = N(x_0,\vec{r}) \exp^{-\tau_\lambda(z_1,z_0)} + \int_{z_0}^{z_1} B_\lambda \exp^{-\tau_\lambda} d\tau_\lambda \qquad (4.9)$$

From the definition of transmittance $\mathcal{T}_\lambda = \exp^{-\tau_\lambda}$ and,

$$d\mathcal{T} = -\exp^{-\tau_\lambda} d\tau_\lambda$$

Equation (4.9) becomes a form of Schwartzchild's equation,

$$N_\lambda(x_1,\vec{r}) = N(x_0,\vec{r}) \exp^{-\tau_\lambda(z_1,z_0)} - \int_{z_0}^{z_1} B_\lambda \, d\mathcal{T} \qquad (4.10)$$

Equation (4.10), or a modified form of it, provides the basis of atmospheric remote sensing. The first term on the right hand side of this equation represents the radiation received at a sensor from a source or target. The second term on the right represents the radiation received at a sensor given off by any intervening atmosphere.

In order to calculate radiance values along any path it will be necessary to integrate both terms over a wavelength interval so (4.10) becomes,

$$N_\lambda(x_1,\vec{r}) = \int_{\lambda_1}^{\lambda_2} \int_{z_1}^{z_0} \Phi_\lambda \, B_{(\lambda,T_1)} \frac{\partial \mathcal{T}}{\partial x} \, dx \, d\lambda + \int_{\lambda_1}^{\lambda_2} \Phi_\lambda \, N_{(x_0,\vec{r})} \exp^{-\tau_\lambda(z_1,z_0)} \, d\lambda \qquad (4.11)$$

where Φ_λ represents a filter function unique to wavelength interval and sensor lens characteristics.

If we confine the use of this equation to a nearly saturated rainshaft, we can make the assumption that the source radiates nearly as a blackbody. As such, the atmospheric radiation can be described using Planck's law or,

$$N_\lambda(x_0,\vec{r}) = \mathcal{E} \, , B_{(\lambda,T_2)}$$

since emissivity, $\mathcal{E}_\lambda \approx 1$, equation (4.11) becomes a common form of Schwartzchild's equation,

$$N_\lambda(x_1, \vec{r}) = \int_{\lambda_1}^{\lambda_2} \int_{z_1}^{z_0} \Phi_\lambda \, B_{(\lambda,T_1)} \frac{\partial \mathcal{T}}{\partial x} \, dx \, d\lambda + \int_{\lambda_1}^{\lambda_2} \Phi_\lambda \, B_{(\lambda,T_2)} \, \mathcal{T}_\lambda \, d\lambda \qquad (4.12)$$

where T_1 is the temperature of the intervening atmosphere and T_2 is the temperature of a black body target.

For ease of calculation we can transform Planck's law from wavelength form to wavenumber form. Since,

$$B_{(\lambda,T)} = C_1 \int_\lambda^\infty \frac{1}{\lambda^5 \exp^{\frac{C_2}{\lambda T}} - 1} \, d\lambda$$

and C_1 and C_2 are Planck's constants. If $\lambda = \frac{1}{\nu}$ then $d\lambda = -\frac{1}{\nu^2} \, d\lambda$. Now, substitute $d\lambda$ into the above equation to get,

$$B_{(\nu,T)} = \int_\infty^\nu \frac{C_1 \nu^3}{\exp^{\frac{C_2 \nu}{T}} - 1} \, d\nu$$

Taking the equation out of integral form,

$$B_{(\nu,T)} = \frac{C_1 \nu^3}{\exp^{\frac{C_2 \nu}{T}} - 1}$$

Equation 4.12 is not yet in working form for MB detection. Since we are not making a complete black body assumption with the microburst, the surface term does not contribute to the total radiance at the sensor and is not used in our MB application. The only time a surface term would come into play is when a mountain or other steep terrain feature would act as a background.

For our situation, only the atmospheric term of Schwartzchild's equation is used. In a scheme developed in the next section, we present a modified radiative transfer equation used exclusively to calculate the radiance received from a microburst embedded horizontal atmosphere. This analytic equation is basically a sequence of the following atmospheric term,

$$N_\nu(x_1, \vec{r}) = \int_{\nu_1}^{\nu_2} \int_{z_1}^{z_0} \Phi_\nu \, B_{(\nu,T)} \frac{\partial \mathcal{T}}{\partial x} \, dx \, d\nu \qquad (4.13)$$

4.1 Radiative Analysis of a Microburst Atmosphere

From Chapter 3, a horizontal microburst atmosphere can be effectively modeled by dividing the atmosphere into 3 separate sections as illustrated by Figure 4.1 .
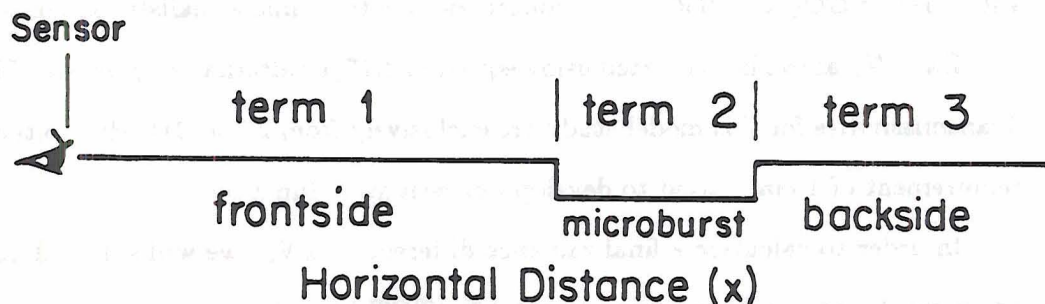
Figure 4.1: Sectorized horizontal microburst atmosphere where the MB is represented as a temperature/moisture discontinuity. Each leg of this atmosphere contributes to the total received radiance described by equation 4.14

The total radiance from such an atmosphere is calculated from the following equation which includes radiative contributions from each three segments of our model. This equation allows for each segment's radiative contribution to pass through each intervening layer of the modeled atmosphere.

$$N_\nu(TOTAL_{MB}) = N_\nu(0 \to MB) + T_\nu(0 \to MB)\, N_\nu(MB)$$
$$+ T_\nu(0 \to MB)\, T_\nu(MB)\, N_\nu(0 \to \infty) \tag{4.14}$$

Term 1 $\to$ The first leg of the model represents the intervening atmosphere; the atmosphere between the sensor and the MB.

Term 2 $\to$ The second leg represents the MB discontinuity. This is characterized by a minimum drop in temperature of $2°$ K, and normally includes an increase in water vapor content as compared to the ambient atmosphere. The radiance from this section must pass thru the intervening atmosphere on its way to the detector and so is altered by $T_\nu(O - MB)$.

Term 3 → The third leg represents the atmosphere "behind" the MB and is assumed to have the same optical characteristics as that of leg 1. However, the radiance calculated from this leg is altered by $T_\nu(O - MB)$ and $T_\nu(MB)$ from the total intervening signal path.

In our model calculations we will assign state variables to each of the three legs along with specific CO_2 and H_2O vapor concentrations to mimic a realistic atmosphere.

Each N_ν above is calculated using equation 4.13, or alternatively by use of FASCOD2. Transmissivities for this model study are exclusively from FASCOD2 due to the resolution requirement of $1\ cm^{-1}$ used to develop our weighting functions.

In order to calculate a final radiance difference (ΔN_ν) we will subtract the radiance produced by the ambient environment ($N_\nu(TOTAL_{env})$) from that radiance generated by the MB atmosphere, $N_\nu(TOTAL_{MB})$. This graphed difference will hopefully show a marked increase (or hump) when our weighted ΔN_ν is calculated at each scanning frequency.

The final radiance difference is then determined by the following equation,

$$\Delta N_\nu = N_\nu(TOTAL_{MB}) - N_\nu(TOTAL_{env}) \tag{4.15}$$

4.2 Weighted Atmospheric Transmissivity

We have chosen to use the near wing of the 15μ CO_2 absorption band for our study. The transmission range from approximately 12.5μ to 15.0μ (650 to 840 cm^{-1}), shows much promise based on the following considerations:

1. The edge of this particular CO_2 band is more nearly a smooth function than the edges of the 4.3μ or 6.3μ absorption bands. This creates an opportunity for selection of a wavelength interval that can be varied in width, yet not drastically change in transmission value. In other words, if the system requires a certain value of transmittance but also requires a wider bandwidth for increased input power needs,

we may likely be able to increase the bandwidth without significantly changing our selected transmittance value.

2. This wing of the 15μ band is spread out over a fairly wide wavelength area and so provides a more gradual spectral transition from the highly opaque region near 15μ to the highly transparent region near 12.5μ. As previously mentioned, better range discrimination is the result. We will select transmissivities and establish weighting functions, $\partial T / \partial \ln x$, that will allow us to define a "look distance" to use in equation (4.13). Again, our look distance is defined as the distance away from a sensor from which maximum radiation is received (see also Kuhn and Kurkowski, 1983). This method of ranging is similar to that used in the retrieval of atmospheric temperature profiles from satellites (Kidder and Vander Haar, to be published).

3. In a clear atmosphere this region of the spectrum is very energy dense. Relative Planck radiance is large near this absorption band when compared to other regions of the IR spectrum (Smith, 1972).

4. Finally, this CO_2 band is less contaminated by other atmospheric constituents than other bands. Except for water vapor, CO_2 is the only significant absorber in the band.

Before we can use equation (4.15) to model a given horizontal atmosphere, we must first establish accurate transmission values. Atmospheric transmission describes how much radiation will be allowed thru the atmosphere and implicitly will enable us to establish pre-determined weighting functions. Since

$$T_\lambda = \exp^{-\tau_\lambda}$$

and from Beer's Law , optical depth is again defined as $\tau_\lambda = \kappa_\lambda \rho_{air} x$ so

$$T = \exp^{-\kappa_\lambda \rho_{air} x}$$

where ρ_{air} represents the density of air containing given amounts of CO_2 and H_2O along

the pathlength. Differentiating the above equation with respect to x yields

$$\frac{\partial \mathcal{T}}{\partial x} = -\kappa_\lambda \, \rho_{air} \, \exp^{-\kappa_\lambda \, \rho_{air} \, x}$$

If we multiply both sides by x, this becomes,

$$\frac{\partial \mathcal{T}}{\partial \ln x} = -\kappa_\lambda \, \rho_{air} \, x \, \exp^{-\kappa_\lambda \, \rho_{air} \, x}$$

and, by substituting the definition for $\mathcal{T}_\lambda$ our weighting function can be mathematically defined as,

$$\frac{\partial \mathcal{T}}{\partial \ln x} = -\mathcal{T} \ln \mathcal{T} \tag{4.16}$$

where the negative sign above comes, once again, from the negative relation between $\mathcal{T}$ and increasing values of x.

Calculated weighting functions for two selected water vapor concentrations are shown in Figure 4.2. As atmospheric transmission decreases with increasing water vapor concentration (4.2A and 4.2B), the peaks of the functions become more discrete and maximized at closer range from the radiometer sensor. We will use some of the same centered frequencies with variable atmospheric concentrations of CO_2 and H_2O to calculate radiance values from our microburst atmosphere.

Centered frequency values that correspond with maximum transmission values within the 650 to 840 cm^{-1} range are selected (Figure 4.3). This will minimize complete attenuation of a signal when large water vapor concentrations are present in the ambient atmosphere and let us "see" as far out as possible.

4.3 General Absorption Characteristics

Factors in equation 4.13 are functions of transmittance, wavelength, and temperature. Wavelength will be an assigned variable and once chosen by the system designer, it will not change. Also, temperature and pressure are easily determined state variables that can be simply measured or assigned.

38

Weighting functions calculated at the following centered wavenumbers
for an atmosphere containing 5 g/kg H2O vapor, from left to right :
717.375, 724.625, 746.375, 750.5, 758.375, 763.25, 772.0, 782.375, & 788.75.
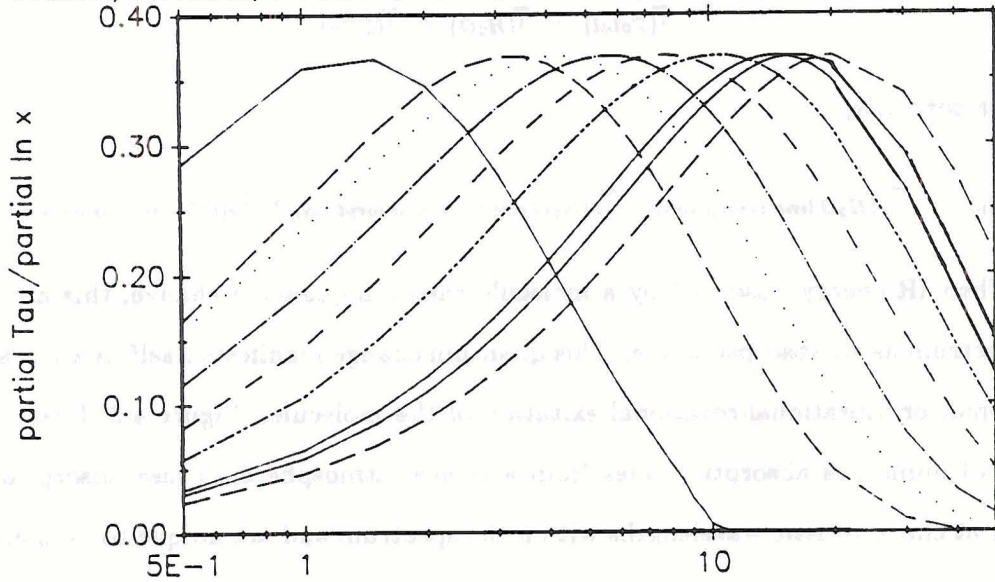
Weighting functions calculated at the following centered wavenumbers
for an atmosphere containing 15 g/kg H2O vapor, from left to right :
750.5, 788.75, 833.875, & 844.5.
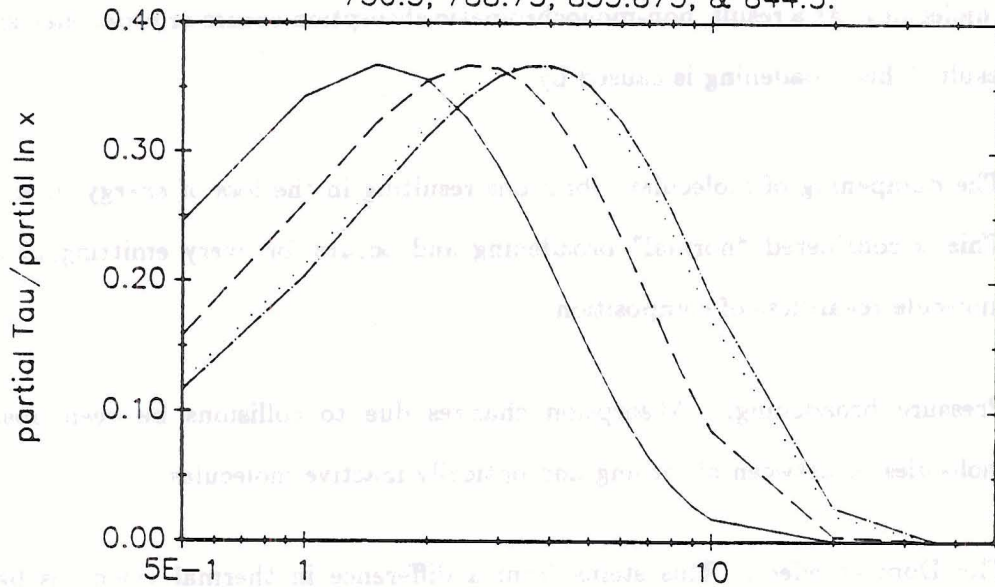
Horizontal Distance (x) in Kilometers

Figure 4.2: 4.2A thru 4.2B are calculated weighting functions for a horizontal atmospheric path. Water vapor content is 5 g/kg for A, and 15 g/kg for B. CO_2 concentration for both sets are 350 ppmv, pressure is 740 mb, and temperature is 293 K. Centered frequency values are picked along the wing of the 15μ absorption band to yield the given ranges. Bandwidth is 1 cm^{-1}, transmissions were calculated using FASCOD2, then input into eqn 4.16 .

Transmissivity is a more complicated story. For our purposes, total atmospheric transmittance is defined as

$$T_{(Total)} = T_{(H_2O)} \times T_{(CO_2)}$$

or more correctly,

$$T_{\nu(Total)} = T_{\nu(H_2O\ line\ absorption)} \times T_{\nu(H_2O\ continuum\ absorption)} \times T_{\nu(CO_2\ line\ absorption)} \quad (4.17)$$

When IR energy absorbed by a molecule causes a quantum change, this appears in the spectrum as an absorption line. This quantum change manifests itself as a vibrational, rotational, or vibrational-rotational exitation of the molecule. Figure 4.3 illustrates the effects of numerous absorption lines from a typical atmosphere. These absorption lines appear at characteristic wavelengths within the spectrum and are unique to each absorber type.

Energy levels during these transitions are frequently altered due to external influences on the molecules. As a result, non-monochromatic absorption occurs or broadened spectral lines result. This broadening is caused by:

1. The dampening of molecular vibrations resulting in the loss of energy in emission. This is considered "normal" broadening and occurs for every emitting/absorbing molecule regardless of composition.

2. Pressure broadening. Absorption changes due to collisions between absorbing molecules or between absorbing and optically inactive molecules.

3. The Doppler effect. This stems from a difference in thermal velocities between molecules as they emit or receive a quanta of light. At low altitudes (below 50 km), doppler broadening is small, and effective broadening is chiefly due to pressure or collision effects (Goody, 1964).
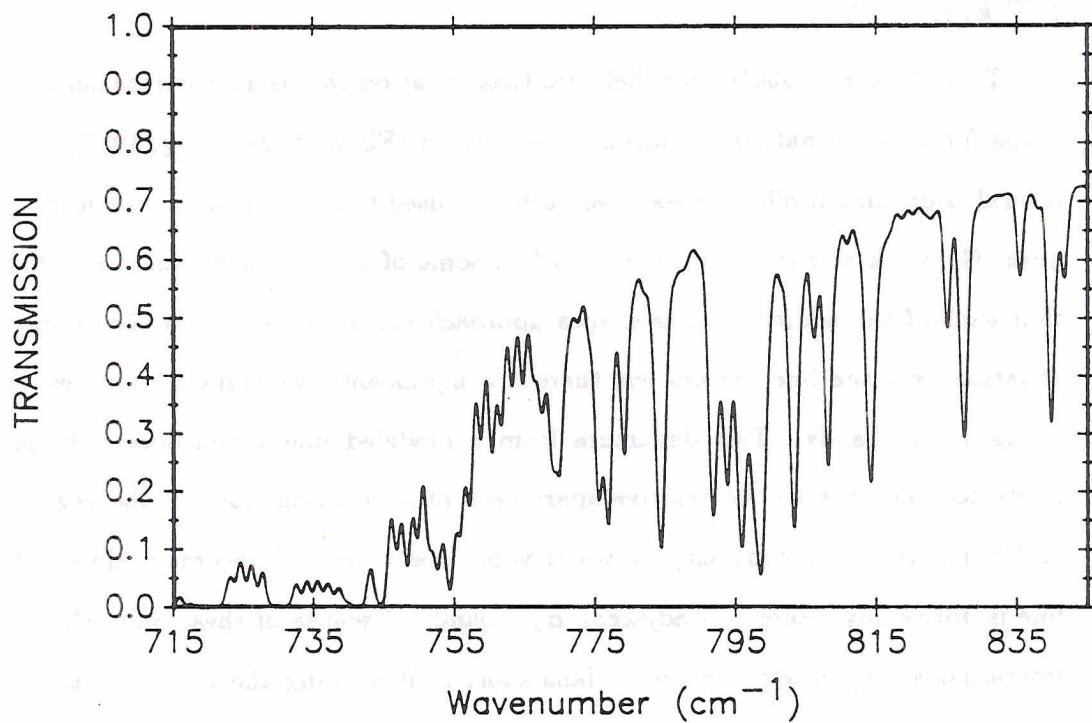
Figure 4.3: Atmospheric transmission lines due to molecular absorption through a 10-km horizontal path. Pressure is 740 mb and T= 293° K. Water vapor mixing ratio is 5 g/kg with 350 ppmv CO_2, and resolution is at 1 cm^{-1} From FASCOD2.

Traditionally, the shape of these broadened spectral lines is given by the Lorentz profile. From Liou (1980), this profile is expressed by the formula

$$k_{\tilde{\nu}} = \frac{S}{\pi} \frac{\alpha}{(\tilde{\nu} - \tilde{\nu}_0)^2 + \alpha^2} = S f(\tilde{\nu} - \tilde{\nu}_0)$$

, where $k_{\tilde{\nu}}$ is the absorption coefficient, $\tilde{\nu}$ denotes the frequency of an ideal, monochromatic line, α is the half width of the line at the half maximum and is a function of pressure and to a much lesser extent temperature, $f(\tilde{\nu} - \tilde{\nu}_0)$ represents the shape factor of a spectral line, and the line strength or intensity is defined by S where $k_{\tilde{\nu}}$ here is normalized so that $\int_{-\infty}^{+\infty} k_{\tilde{\nu}} \, \partial \nu = S$.

Thru the early 1950's it was believed that equation 16 was an accurate depiction of line shape for most all natural atmospheric absorbers (Elsasser and King, 1952). Since then, several additional profile shapes have been proposed to describe these pressure broadened lines. Gryvnak and Burch (1978) described some of these profile equations. They noted that each of the additional line shapes approach the values given by the simple Lorentz equation near the line centers but there are significant line shape differences on the far wings of the bands. This departure from a modeled line shape dose not appreciably apply to CO_2 due to the relative sparseness of absorption lines in the region (Goody and Yung, 1987). In contrast, the water vapor spectrum includes many lines, where each line is noticeably altered by adjacent H_2O bands. Because of these and other molecular interactions, any single line profile falls short in describing the total character of water vapor transmission thru the atmosphere.

Additional contributions to the total spectrum are believed to come from IR interactions with dimers. For example, minor isotopes of CO_2 provide their own distinct line spectra, but are masked by the more abundant $C^{12}O_2^{16}$ molecule which represents more than 98 percent of all atmospheric CO_2 (McClatchy, et al., 1973).

4.4 CO_2 Absorption

The CO_2 molecule is linear and has one normal mode of vibration in the 650 to 840 cm^{-1} range.

The intense band of CO_2 absorption at 15μ is due to this exclusive vibrational quantum transition. Figures 14 and 15 illustrate the coarse resolution transmission qualities of this CO_2 vibrational mode. Notice the smooth shape of this absorption "wing" and the extreme variations of $\mathcal{T}$ with changing wavelength. This gross feature is called the fundamental band as it is caused by a transition from the molecular ground state to its first excited vibrational state (Liou, 1980). Interactions between this vibrational state and the contribution of a molecular bending mode induces angular rotation in the molecule (McClatchy, *et al.*, 1972). This vibrational-rotational part of the CO_2 spectrum owes its fine structure to the influence of rotational effects on this fundamental vibration state. As these vibrational and rotational lines overlap, more broadened lines are added, making the spectrum even more complicated.

Any absorption thru the atmosphere is dependent on the concentration of the absorbing media in the pathlength. Over the past 6 years, concentrations of CO_2 near the earth's surface have been shown to vary from ≈ 338 parts per million by volume (ppmv) at Niwot Ridge, CO, to in excess of 354 ppmv at the Mauna Loa observatory in Hawaii (Oak Ridge National Laboratory, 1989). Although increased and fluctuating CO_2 concentrations are currently being recorded world wide, we have chosen a fixed value of 350 ppmv as a representative concentration for this MB model study. Seasonal and geographical variations to this approximate concentration will not be considered for this theoretical study.

4.5 H_2O Absorption

As indicated in equation (4.17), total absorption/transmission by water vapor comes from two sources: H_2O line absorption and H_2O continuum absorption. On the wings of the 15μ CO_2 absorption band, we find that water vapor significantly effects atmospheric transmission values and so plays a crucial role in determining total transmittance.

The water vapor molecule is asymmetric with the oxygen atom in the center and a bond angle of ≈ 104.5 deg.

ATMOSPHERIC TRANSMITTANCE

LOWTRAN7 output at a horizontal distance of 1.0 km
with 5 g/kg H2O, 350 ppmv CO_2, 294 K, and 1013 mb.

Source Index
o——o H2O Line
▲——▲ CO2 Line
▲····▲ H2O continuum
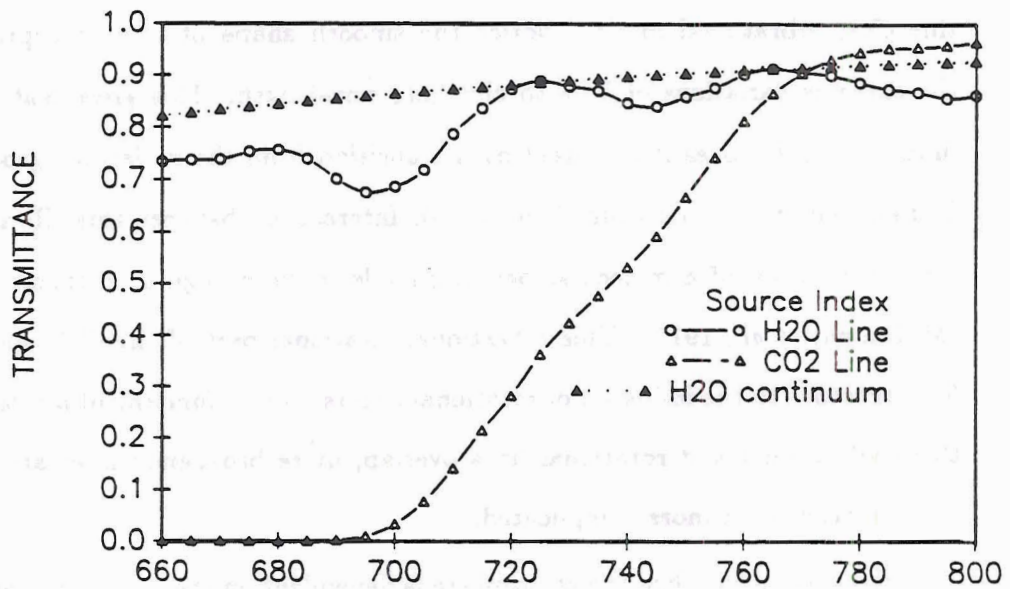
LOWTRAN7 output at a horizontal distance of 10.0 km
with 5 g/kg H2O, 350 ppmv CO_2, 294 K, and 1013 mb.

Source Index
o——o H2O Line
▲——▲ CO2 Line
▲····▲ H2O Continuum

WAVENUMBER (cm**−1)
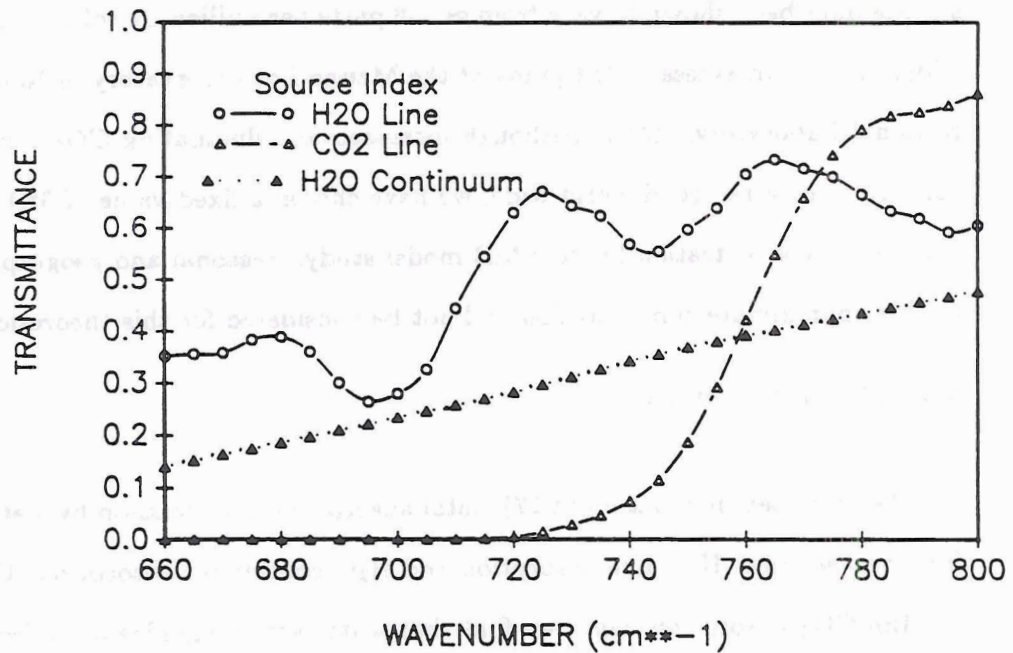
Figure 4.4: The near wing of the 15μ absorption band where each absorption/transmission contribution is graphed separately. Atmospheric water vapor is broken up into an absorption line and a continuum contribution. The upper graph is for a pathlength of 1 Km and the lower for 10 Km.

Just like CO_2, water vapor line absorption is described in terms of a finite number of absorption lines. Because of the different molecular configuration, water vapor lines are much more complicated. As described by Goody and Yung, (1989), the vibrational-rotational qualities of this lop sided molecule give rise to a widespread and disorderly array of absorption lines. These properties combine with the highly fluctuating concentrations of water vapor in the lower atmosphere to account for the numerous water vapor lines and intensities in this part of the spectrum. Although not sporadic in position, these water vapor lines vary in intensity based on the amount of moisture in an observed pathlength.

As previously noted, atmospheric attenuation from water vapor in most all far infrared regions is actually greater than predicted from calculations of Lorentzian absorption line contributions. This extra absorption is called continuum absorption as it represents a significant depression of the spectral background in the regions between absorption lines. Burch and Gryvnak,(1980) have shown that unlike actual line intensity, the H_2O vapor continuum is somewhat frequency independent and is directly linked to the amount of water vapor along the absorbing path. Figures 4.4 shows the effects of the water vapor continuum for the given atmospheres.

Work by Gryvnak and Burch (1978), and Clough,*et al.*,(1980), suggests that the continuum can be represented by considerable modification to traditional line shape theory. New lines profiles would need to be very versatile. For example, self broadened H_2O lines are modified because H_2O molecules collide with other H_2O molecules. These broadened line shapes are apparently different than N_2 broadened H_2O lines. This makes a single Lorentzian like profile inadequate to describe water vapor absorption characteristics as it could describe only one of these broadened profiles. Gryvnak and Burch also noted that the shapes of these extreme line wings show a slight temperature dependence that is not predictable by simple line shape theory.

Nordstrom and Thomas (1980), suggest that infrared absorption by dimers or by complex molecular water clusters could be responsible for unresolved H_2O vapor absorption in the far wings. They argue that even though the relative concentrations of these absorbers are small, their contribution to total absorption could be significant.

Regardless of the exact mechanism, water vapor continuum effects are coupled with modeled H_2O line profiles to accurately asses the effect water vapor has on total atmospheric transmittance. In simpler terms, this continuum effect represents an error factor that is added to the consistently low values of absorption form mere line calculations.

Unlike CO_2, H_2O vapor concentration is extremely variable in the lower troposphere and atmospheric transmission changes are largely due to these variations. Any IR sensor operating in this spectral region must therefor be able to effectively "look" in areas of the CO_2 absorption band where the atmosphere will transmit the desired amount of radiation based on weighting function requirements and the amount of water vapor in the atmosphere. Continuum effects on atmospheric transmission are taken into account in both the LOWTRAN7 and FASCOD2 programs used in this study (see appendix).

Chapter 5

MODEL OUTPUT RESULTS

This chapter presents radiance characteristics of various modeled microburst atmospheres as quantified by equation 4.15 . Each of the ΔN graphs in this chapter represent radiance differences calculated as a function of wavenumber (cm^{-1}). As a reminder, wavenumber is the inverse of wavelength so increased wavenumber means a decreased wavelength. This is worthwhile to mention as we will be discussing wavenumber characteristics of modeled atmospheres without referring to wavelength.

In Figures 5.1 and 5.2, we will express this wavenumber as a "look" distance (in Km) representing a theoretical distance from the detector; this is an effort to show how close our positioned MB ΔN maximum comes to the pre-determined look distance. As a reminder, actual centered wavenumber values are selected to coincide with previously determined weighting functions for a given atmosphere (Chapter 4). All calculations are using a centered bandwidth of 1 cm^{-1}.

Other than Figure 5.1 and 5.2, it is more conceptually accurate to discuss our scanning technique in terms of direct wavenumber as each wavenumber scan contains some information about all physical ranges in our field of view. As we shall soon see, our weighting function does not necessarily represent a discrete physical distance as Figure 5.2 graphically illustrates.

Furthermore, this chapter concentrates on a limited number of MB scenarios. For our study we restrict our MB horizontal width to 2 Km, and we place the MBs at distances of 5 and 10 Km from our theoretical sensor. CO_2 concentration is fixed at 350 parts per million by volume.

In order to asses the detectability of a MB based on its thermal difference we need first to establish typical atmospheric values to use in our radiance calculations. Sinclair

and Kuhn (1990) have made flight level penetration studies of high plains MBs. They determined that during their MB penetrations (approximately 1600 ft AGL), the average ambient temperature is $\approx$ 293 ° K at a typical flight level pressure of 740 mb. During MB penetration, temperature drops were observed to range from about 2 to 6 ° K. So, in order to asses the detectability of a MB based on its thermal difference we have chosen to mimic these general characteristics in our hypothetical atmosphere. Most of our MB modeling assigns a minimum ΔT of –2 ° K as compared to the ambient environment. This choice is based on the logic that if we can detect a MB of only –2 ° K, then we can certainly detect the colder MBs using our differencing technique. In some model runs ΔT_{mb} was set to –10° K in order to depict the ΔN trace that may be associated with a more intense MB. The ambient environmental temperature (293 ° K) is fixed for all our model runs.

Before we discuss radiative properties of the most realistic atmospheric scenarios, it is pertinent to first discuss the general effect of temperature and water vapor fluctuations within a MB atmosphere.

5.1 Temperature and Water Vapor Effects on a MB Atmosphere

To provide a fundamental understanding of radiance variations caused by an embedded MB, we will first analyze a theoretical MB that is defined by a temperature difference only. In our first case, the ambient atmosphere and the MB both contain 0 g/kg H_2O vapor and the MB ΔT is varied as shown in Figure 5.1.

Since, in this case, we have centered the MB at a range from the sensor that coincides with a predetermined weighting function, we are able to calculate a maximum radiance difference (ΔN) at this location. This yields a maximum or "peaked" value as shown. Also graphed are the effects of a colder MB (from $\Delta T = -2$ to $-4°K$). A colder MB, naturally, produces a larger ΔN anomaly and consequently is easier to detect.

The addition of water vapor to our hypothetical atmosphere dramatically changes the ΔN signature. Figure (5.2) represents graphed model output results where the MB has a fixed ΔT of –2 ° K and the water vapor concentration is varied within the MB. The environmental mixing ratio (w_{env}) still remains at 0 g/kg H_2O.
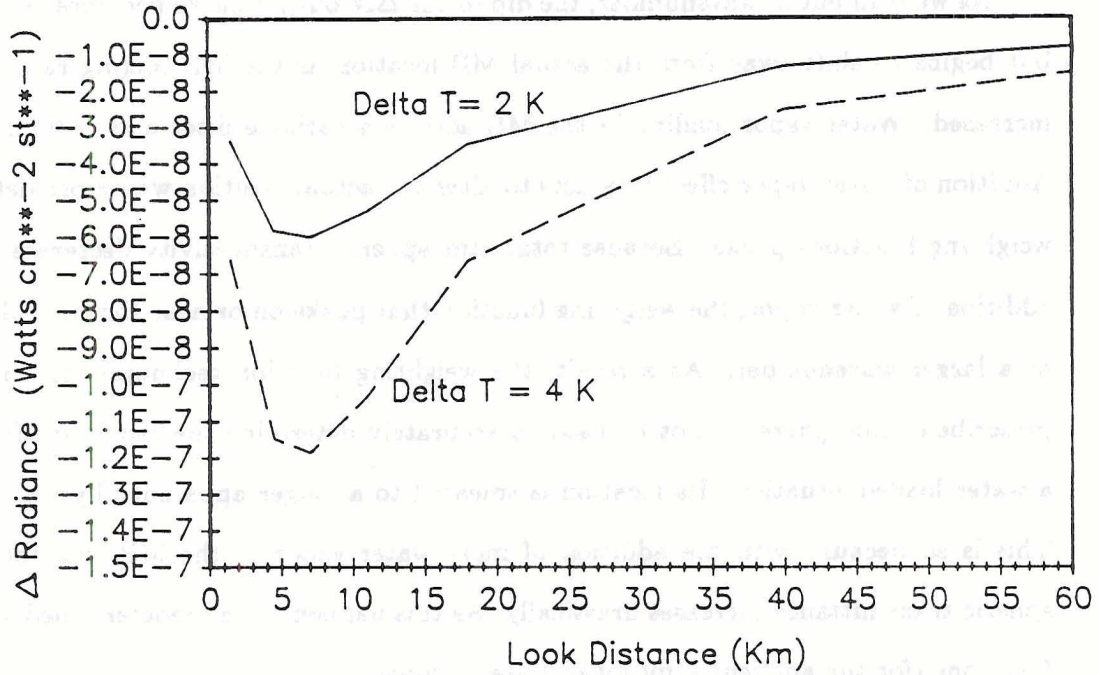
Figure 5.1: ΔN from a hypothetical MB atmosphere where there is no water vapor in the environment or the MB. The MB is physically centered at 5 Km from the sensor.
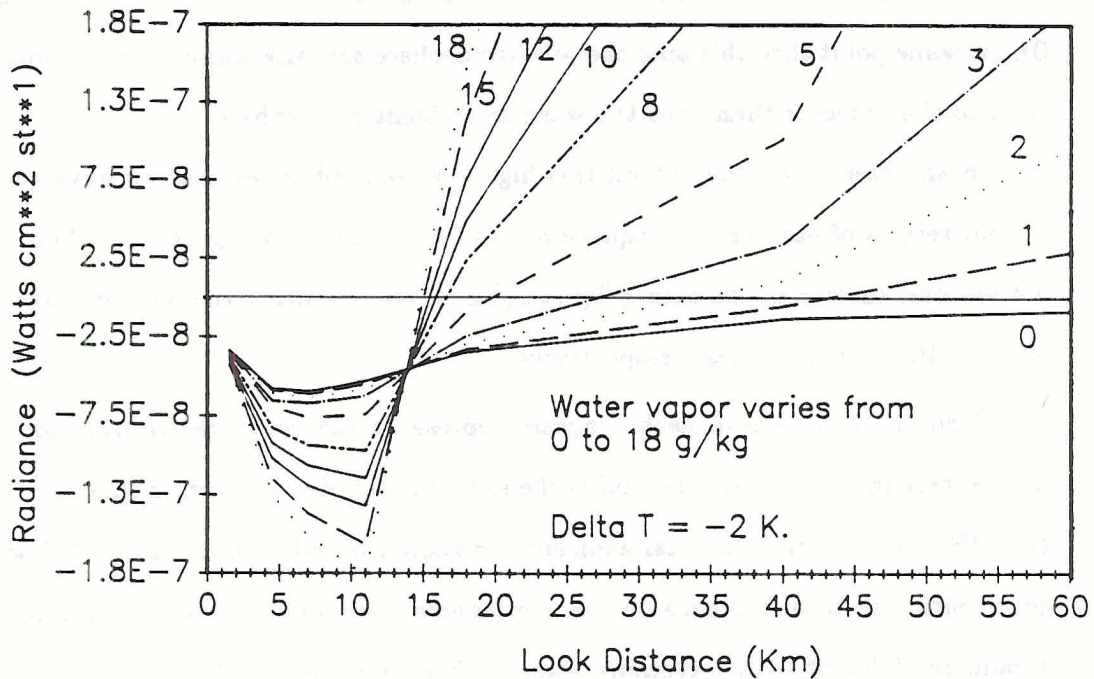

Figure 5.2: ΔN from a hypothetical MB atmosphere where the water vapor in the environment is fixed at zero and ΔT is a constant $-2°$ K. Water vapor varies as shown and the MB is centered at ≈ 5 Km.

As we scan out in wavenumber, the dip in the ΔN output curve becomes very distinct but begins to shift away from the actual MB location as the MB mixing ratio (w_{mb}) is increased. Water vapor loading in the MB acts as a variable filter and radiance source. Addition of water vapor effectively acts to alter the actual position where pre-determined weighting functions peaks. Because total atmospheric transmissivity decreases with the addition of water vapor, the weighting function that peaks on or near the cold MB is now at a larger wavenumber. As a result, the weighting function technique for an initially prescribed atmosphere cannot be used to accurately determine the range to MB in such a water loaded situation. Its location is smeared to a longer apparent physical distance. This is so because with the addition of more water vapor in the MB, the total atmospheric transmittance increases drastically. As this happens, the predetermined weighting functions (for the ambient atmosphere) are no longer valid.

As the "look" distance increases in Figure 5.2 (i.e the variation in frequencies to wavelengths at which the atmosphere is more transparent), a dramatic reversal occurs. The ΔN begins to decrease in absolute value until a crossing of the null axis occurs ($\Delta N_{\dot{c}}$ 0). At some point thru this scan the MB atmosphere actually seems to yield more radiance back to the detector than does the warmer ambient atmosphere.

In an attempt to understand this higher wavenumber reversal we have graphed the output results of each term in equation 4.14 for two cases in Figure 5.2 . Figures 5.3 and 5.4 are breakdowns of the zero g/kg (w_{mb}) case (representing the ambient atmosphere), and the 10 g/kg (w_{mb}) case, respectively.

Term 1 (solid line)in each diagram represents the radiance contribution from the atmosphere in front of the MB and is the same in each figure. Term 2 (dashed) represents the MB's contribution to total atmospheric radiance and term 3 (dotted) describes the contribution to total radiance by the atmosphere "behind" the MB. In each graph, Term 1 radiance falls off with increasing wavenumber as expected. As we look further out in wavenumber, we actually see less of this section and therefore receive less radiance.

The contribution from Term 2 in both graphs show markedly different signatures based on the effect of the added water vapor. As wavenumber increases in the 10 g/kg
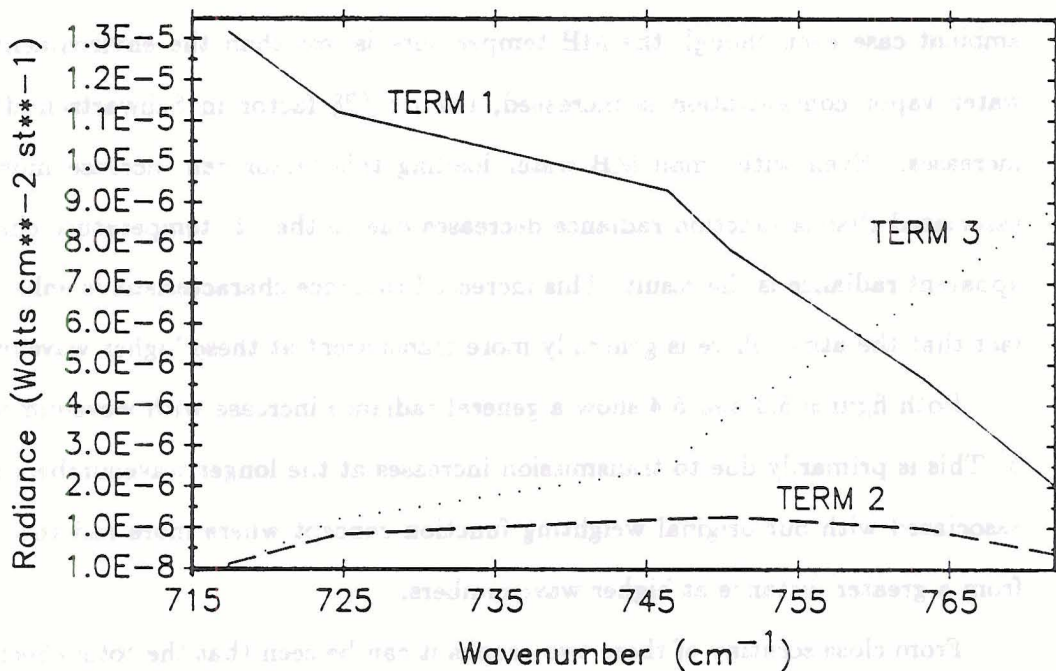
Figure 5.3: Radiance calculated from the three individual terms of equation 4.14 as a function of wavenumber for a conceptual MB atmosphere described in figure 5.2 . This graph depicts the reference or ambient atmosphere radiance breakdown.(See text)
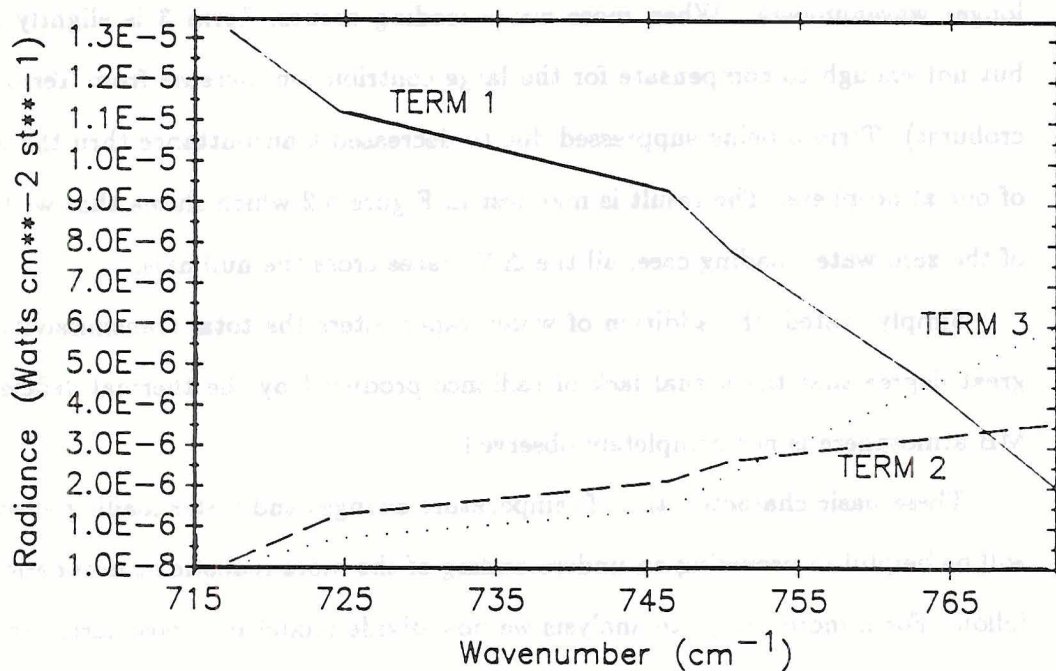

Figure 5.4: As in Fig 5.3 above but for an atmosphere where the MB is loaded with 10 g/kg H^2O, ΔT also equals $-2°$ K.

water vapor case we observe a noticeable increase in received radiance compared to the ambient case even though the MB temperature is less than the environment. Because water vapor concentration is increased, the $\partial T/\partial x$ factor in Schwartzchild's equation increases. Even with small MB water loading this factor can increase more than the associated Planck function radiance decreases due to the $-2°$ temperature change. More apparent radiance is the result. This increased radiance characteristic is enhanced by the fact that the atmosphere is generally more transparent at these higher wavenumbers.

Both figures 5.3 and 5.4 show a general radiance increase with wavenumber in Term 3. This is primarily due to transmission increases at the longer wavenumbers and can be associated with our original weighting function concept where more radiance is received from a greater distance at higher wavenumbers.

From close scrutiny of these two graphs it can be seen that the total effect of Term 2 + Term 3 is significantly greater in the 10 g/kg case than the ambient atmosphere case, especially at the higher wavenumbers. As the MB water vapor content is increased, Term 2 becomes a larger contributor with the most drastic contribution change coming at the longer wavenumbers. When more water loading occurs, Term 3 is slightly suppressed but not enough to compensate for the large contribution increase from Term 2 (the microburst). Term 3 being suppressed due to decreased transmittance thru the MB section of our atmosphere. The result is manifest in Figure 5.2 which shows that with exception of the zero water loading case, all the ΔN traces cross the null axis.

Simply stated, the addition of water vapor alters the total transmissivity to such a great degree that the actual lack of radiance produced by the thermal deficiency of the MB atmosphere is not completely observed.

These basic characteristics of temperature changes and water loading effects on ΔN, will be helpful in providing an understanding of the more realistic atmospheric cases that follow. For a more complete analysis we now divide modeled atmospheric cases into two categories: (1) high plains or "dry" MB atmospheres and (2) south east United States MBs that appear to be more water saturated than the high plains variety.

5.2 High Plains Microbursts

Atmospheric values of temperature, pressure, and CO_2 concentrations previously defined are characteristic of those in a high plains MB atmosphere. The Sinclair and Kuhn (1990) airborne study found that average water vapor mixing ratios in typical Colorado MBs were approximately 4-5 g/kg in the ambient environment (w_{env}), and 6-8 g/kg in the MB shaft (w_{mb}).

In order to examine a more complete range of water vapor variations we have modeled high plains MB atmospheres where w_{env} is set at 3, 5, and 8 g/kg and w_{mb} is varied as indicated in the following figures. Each MB is physically placed at 5 and 10 Km for each w_{env} test case.

5.2.1 Environmental Mixing Ratio of 3 g/kg

Figures 5.5 and 5.6 illustrate model output for atmospheres representing a minimum amount of expected water vapor; even for the high plains area. With water vapor concentrations having a relatively small difference effect at the lower wave numbers we note in both these graphs that there is a distinct cross-over between the 5 and 6 g/kg trace. At wavenumbers prior to this cross- over point the temperature difference of the 5 g/kg MB is a greater contributor than the 6 g/kg case is a detractor. However, with any further water loading, the Planck function temperature dominance becomes totally swamped by water vapor loading. Although not very discrete, both these curves show noticeable peak values in ΔN with a minimum absolute value of $\approx 4.5 \times 10^{-8}$.

With the MB placed at 5 km (Fig. 5.5) we notice more detail in the signatures. This is due to the atmospheric transmission decrease in the 10 km case (Fig. 5.6). Because the 10 km MB radiance must travel thru more atmosphere, the signal is smoothed and attenuated which shifts the peak ΔN value with respect to the 5 km case. This turns out to be the most well defined peak value of ΔN of all our realistic atmospheres. Because we have a minimum amount of water vapor influencing our desired radiance reception these traces seem logical when comparing this case with Figure 5.1 where we had zero ambient water loading.

Figure 5.5: ΔN where atmospheric water vapor is 3 g/kg and the MB is loaded with 5, 6, and 7 g/kg water vapor. Microburst is centered at 5 km. ΔT_{mb}= -2° K.
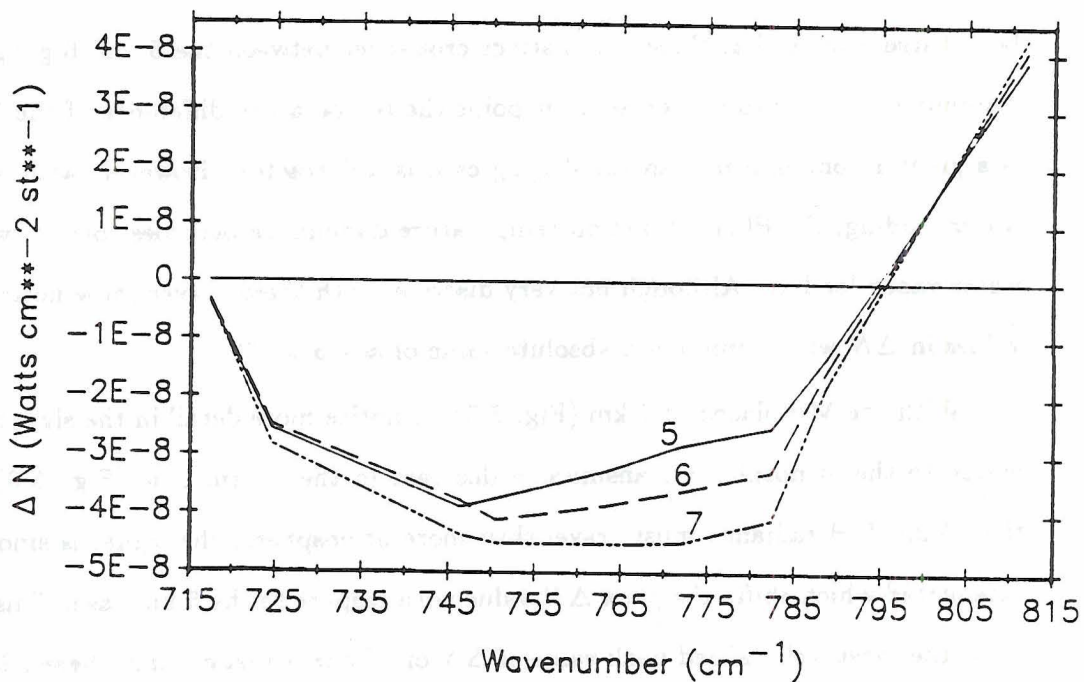
Figure 5.6: ΔN where atmospheric water vapor is 3 g/kg and the MB is loaded with 5, 6, and 7 g/kg water vapor. Microburst is centered at 10 km. ΔT_{mb}= -2° K.

5.2.2 Environmental Mixing Ratio of 5 g/kg

This case represents perhaps the most typical high plains MB atmosphere. This dry MB scenario illustrates many of the attributes of the dryer 3 g/kg case with a few exceptions. Due to the increased water loading of both the environment and the MB, the ΔN signatures have less distinct peak values as shown in figures 5.7 and 5.8. Since the percentage difference of this loading is much smaller than in the previous case it seems logical that both transmission and radiance characteristics would be less abrupt in this atmosphere. Nevertheless, the peaked segment that roughly correlates with the MB location is still noticeable in the 5 km graph (Fig. 5.7), and attains a value on the order of 10^{-8} radiance units.
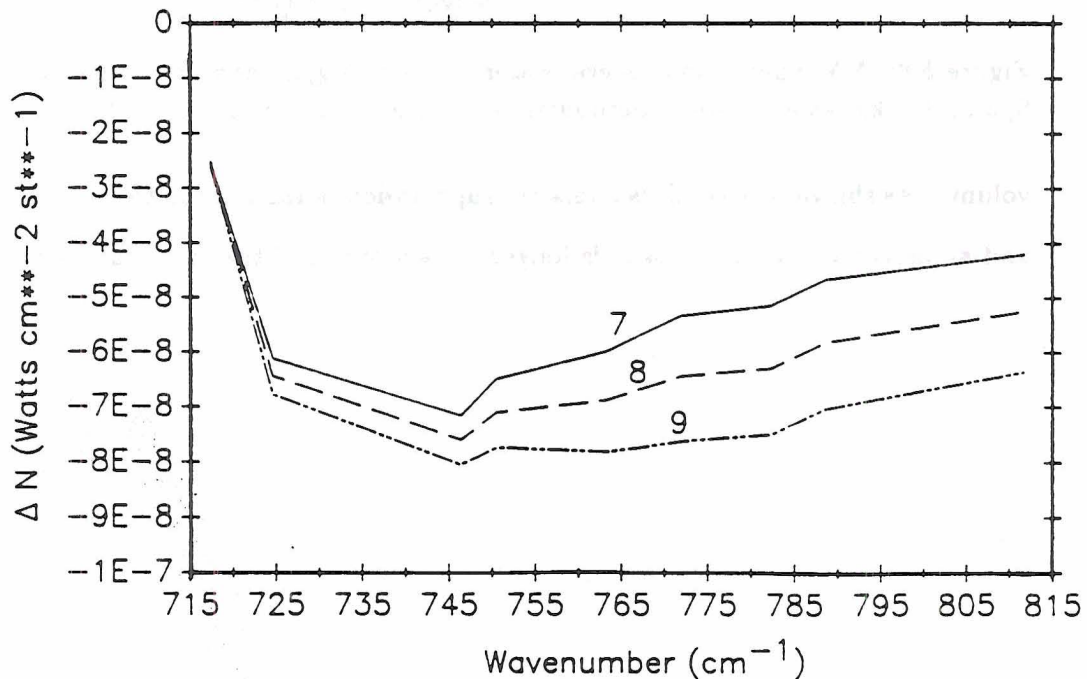
Figure 5.7: ΔN where atmospheric water vapor is 5 g/kg and the MB is loaded with 7, 8, and 9 g/kg water vapor. Microburst is centered at 5 km. $\Delta T_{mb} = -2°$ K.

Figure 5.8 is a model run for this same atmosphere where we have increased our ΔT to $-10°$ K; a much colder MB. The signatures are similar to that of the -2 ° K case at 5 km with a shift in the wavenumber position of the maximum ΔN value and nearly an order of magnitude increase in its absolute value. As MB temperature decreases, it results in a density increase which is translated to a slight transmission decrease thru the the MB
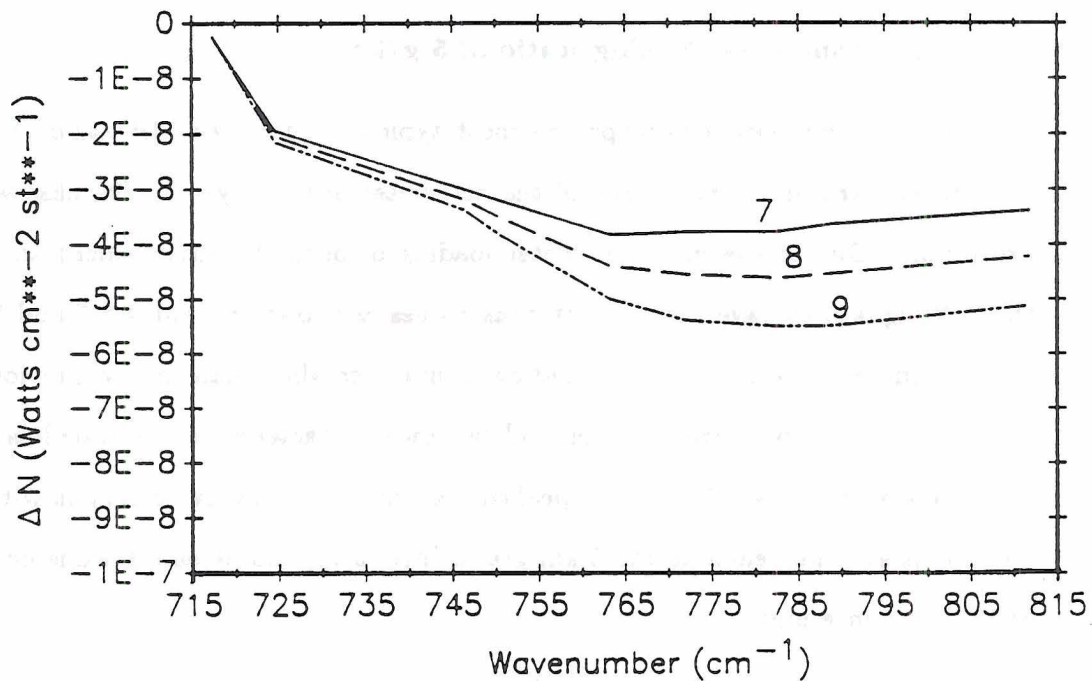
Figure 5.8: ΔN where atmospheric water vapor is 5 g/kg and the MB is loaded with 7, 8, and 9 g/kg water vapor. Microburst is centered at 5 km. $\Delta T_{mb} = -10°$ K.

volume. As shown, the result is a relative suppression of radiance in the near wavenumbers and an associated shifting towards longer wavenumbers of the ΔN maximum.

5.2.3 Environmental Mixing Ratio of 8 g/kg

The last example in the high plains category is the most dense in water vapor (Figures 5.9 and 5.10). This possible water loading case yields the largest values of ΔN yet calculated. This is apparently the case because water vapor is at an optimal concentration to act as a source but not at an optimal concentration yet to attenuate the bulk of the emitted and transmitted atmospheric radiance signal. The signatures are smooth and still show a gradual peak in the mid wavenumber region.
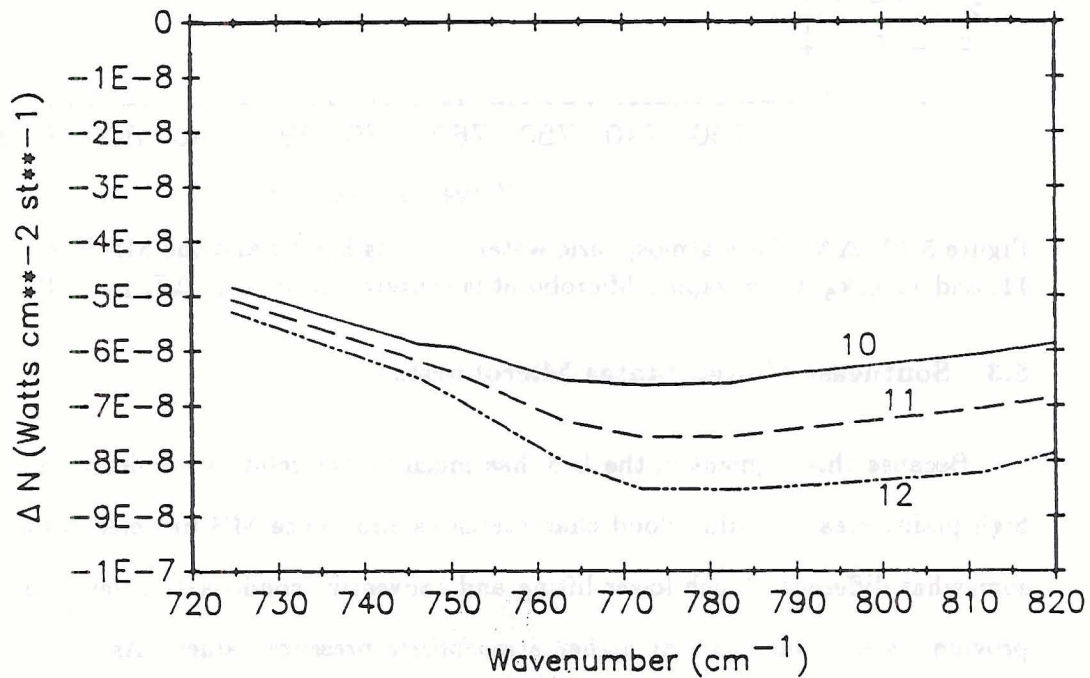

Figure 5.9: ΔN where atmospheric water vapor is 8 g/kg and the MB is loaded with 10, 11, and 12 g/kg water vapor. Microburst is centered at 5 km. $\Delta T_{mb} = -2°$ K.

As compared to the earlier less saturated model runs, the mixing ratio traces are now noticeably closer to one another especially in the 10 km plot. As the water vapor concentration goes up (w_{env}), we add a smaller percentage of total water to the theoretical MB . In an absolute sense, the intervening atmosphere contribution and the contribution from behind the MB act to influence the total signature more than MB water fluctuations. Therefore, the slight incremental changes in w_{mb} will have less effect on calculated ΔN signatures.
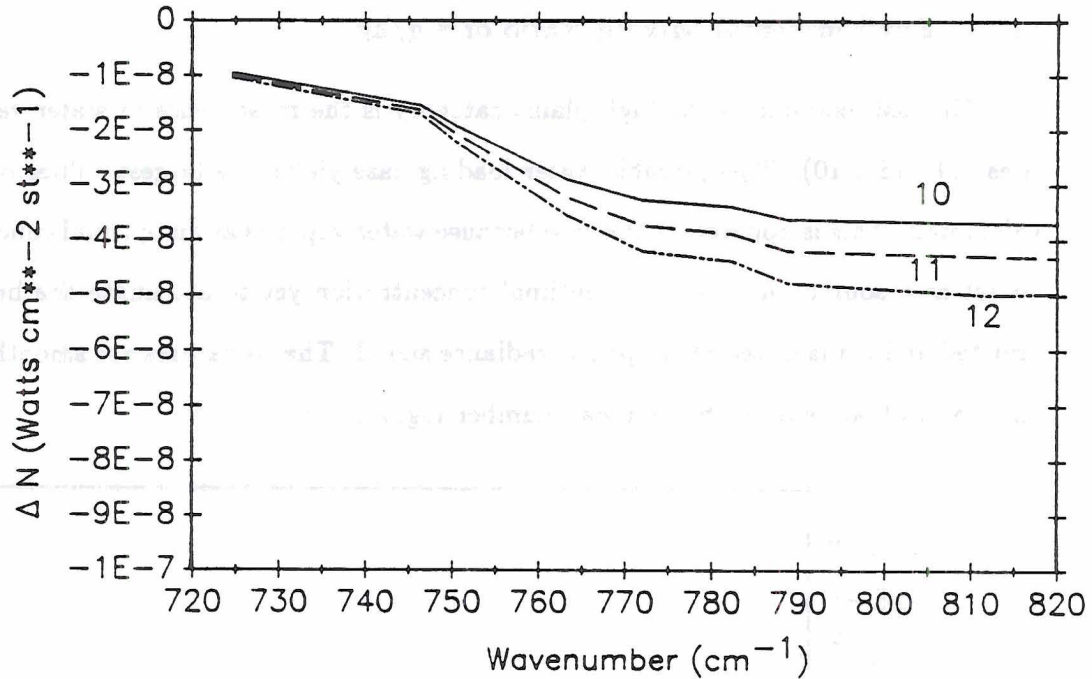
Figure 5.10: ΔN where atmospheric water vapor is 8 g/kg and the MB is loaded with 10, 11, and 12 g/kg water vapor. Microburst is centered at 10 km. $\Delta T_{mb} = -2°$ K.

5.3 Southeast United States Microbursts

Because this segment of the U.S. has much higher relative humidity values than the high plains area, cumulus cloud characteristics and hence MB modeled atmospheres are somewhat different. Much lower lifting and convective condensation levels in this region provide lower cloud bases at higher atmospheric pressure values. As a result, this MB category reflects higher water vapor loading in both the environment and the colder MB coupled with pressure broadening effects in an atmosphere now at 940 mb. The graphed model output in this section differs from that of the high plains only by these pressure and water vapor increases. The ambient temperature remains 293 ° K.

5.3.1 Environmental Mixing Ratio of 12 g/kg

Figure 5.11 and 5.12 show graphed results of MBs model runs where w_{env} is fixed at 12 g/kg and w_{mb} is varied as shown. Calculated ΔN values are still on the order of 10^{-8} with the 10 Km case showing a maximum of about one-third the value of the 5 Km model run. Heavy water loading in this atmosphere coupled with effects of added pressure

broadening (940 mb) make for extremely poor transmissivity, so calculated ΔNs can be greatly suppressed.

In the 5 Km example most of the radiance deficit from the MB is able to get thru the intervening atmosphere and a familiar curve results. There is even the hint of a peaked value at $\approx 790 \text{cm}^{-1}$. This case resembles our most saturated case in the high plain category, but shows a greater slope leading to the maximum ΔN value which is located at a larger wavenumber.
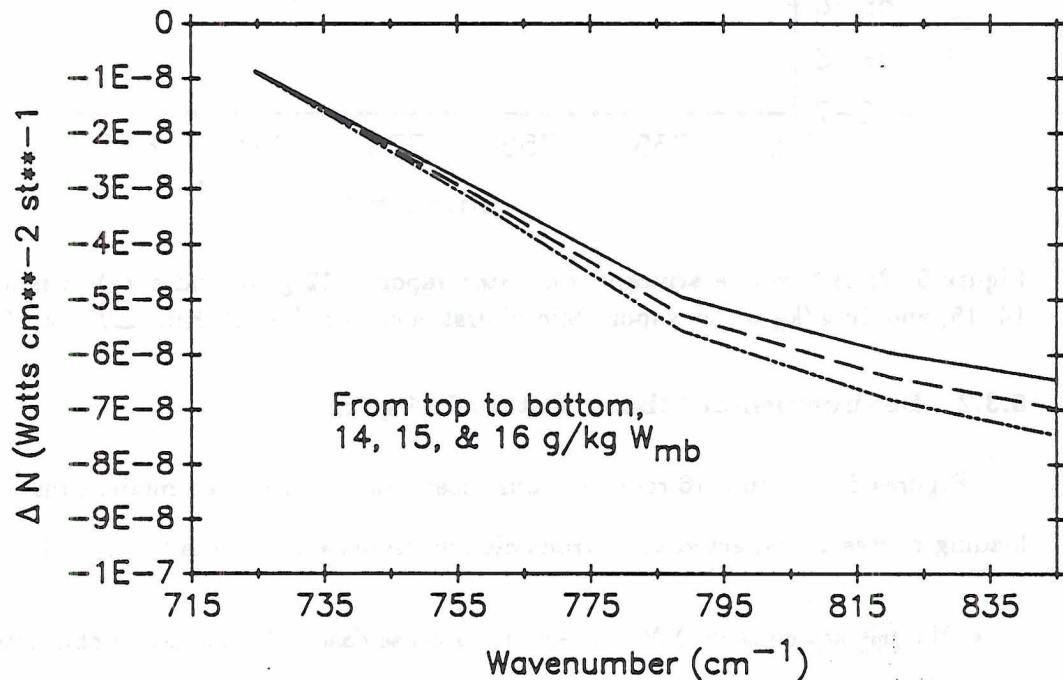
Figure 5.11: ΔN where atmospheric water vapor is 12 g/kg and the MB is loaded with 14, 15, and 16 g/kg water vapor. Microburst is centered at 5 Km. $\Delta T_{mb} = -2° \text{K}$.

It is worthwhile to mention that we are still on the wings of the 15μ CO_2 absorption band where we reach maximum transmission at $\approx 845 \text{ cm}^{-1}$. Keeping this in mind, 845 cm^{-1} represents a maximum range at which we receive the largest contribution of radiance. Using weighting function arguments, this radiance peak occurs at approximately 6 Km for a homogeneous atmosphere containing 12 g/kg water vapor. Knowing this, it is reasonable to expect significantly less ΔN values at the 10 km range where much less of the MB effect can be sensed by the radiometer.
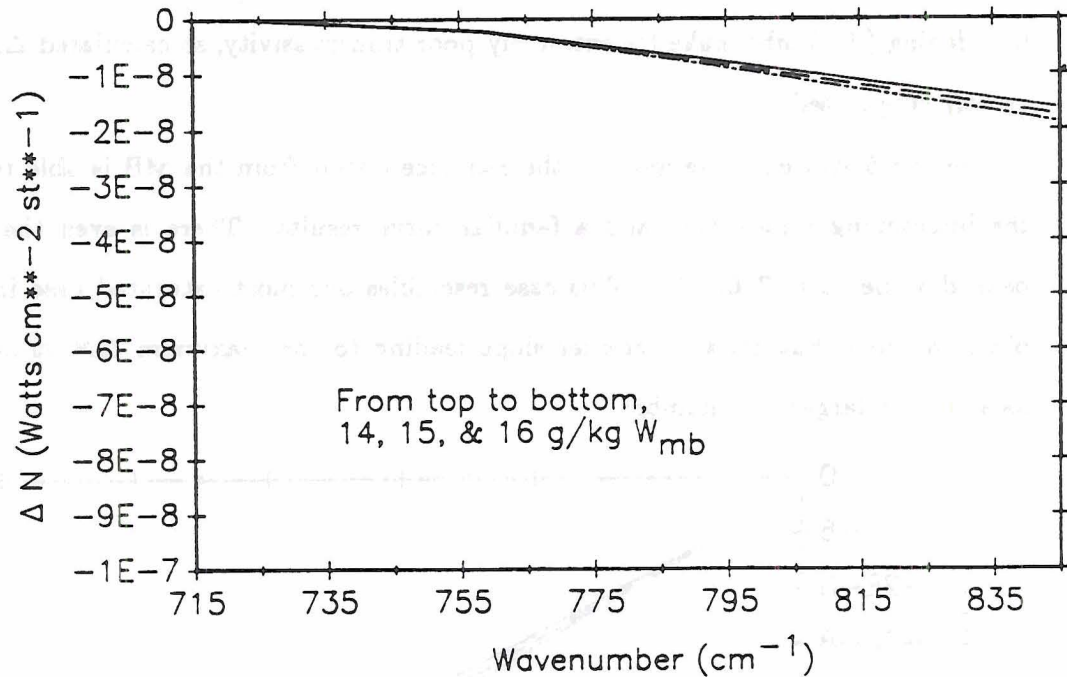
Figure 5.12: ΔN where atmospheric water vapor is 12 g/kg and the MB is loaded with 14, 15, and 16 g/kg water vapor. Microburst is centered at 10 Km. $\Delta T_{mb} = -2°$ K.

5.3.2 Environmental Mixing Ratio of 15 g/kg

Figures 5.13 thru 5.16 represent our most heavily saturated model runs. This heavy loading causes an expected total transmission decrease and leads to the following:

- No distinct peak in ΔN is observed in these cases. Transmission characteristics are so poor that the furthest weighting function peak is centered at $\approx$ 4 Km (see fig. 4.2 B WF for a 15 g/kg atmosphere). So, we are able to see just a small fraction of a MB at 10 km.

- Although the slope of each ΔN trace decreases when compared to the dryer cases, there is still a difference of at least 10^{-8} units in all atmospheres except fig 5.15. This will prove to be important when we consider detectability requirements.

- At these water loading levels ΔT_{mb} decreases can have a significant impact on ΔN, but this effect can only be realized at longer wavenumbers or when the MB is very close to the detector.
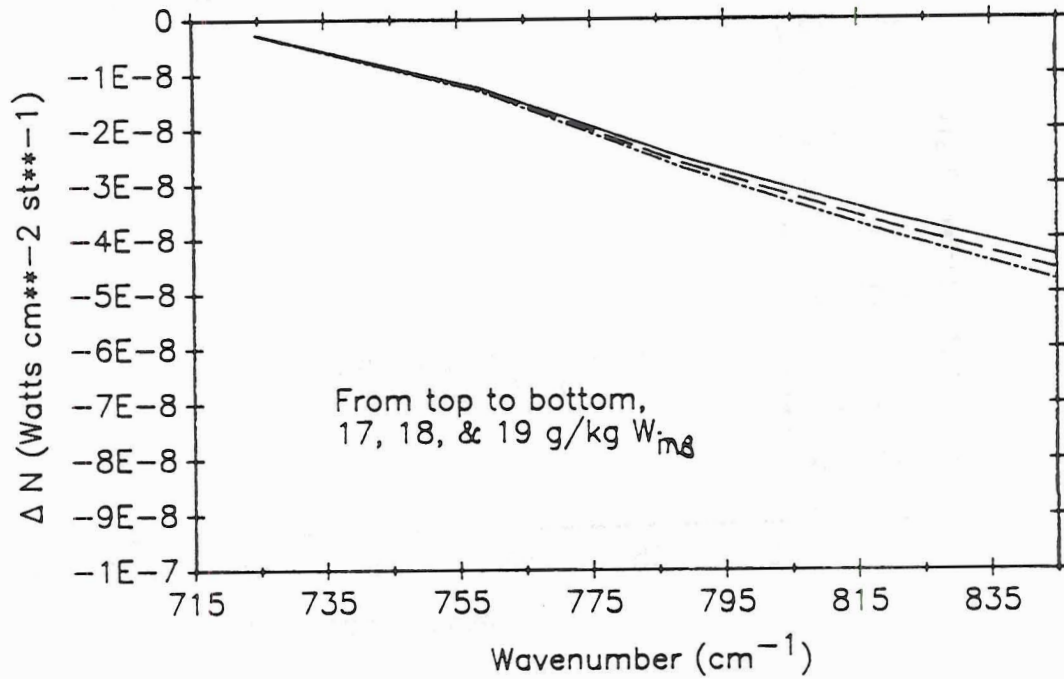
Figure 5.13: ΔN where atmospheric water vapor is 15 g/kg and the MB is loaded with 17, 18, and 19 g/kg water vapor. Microburst is centered at 5 Km and $\Delta T_{mb} = -2°$ K.
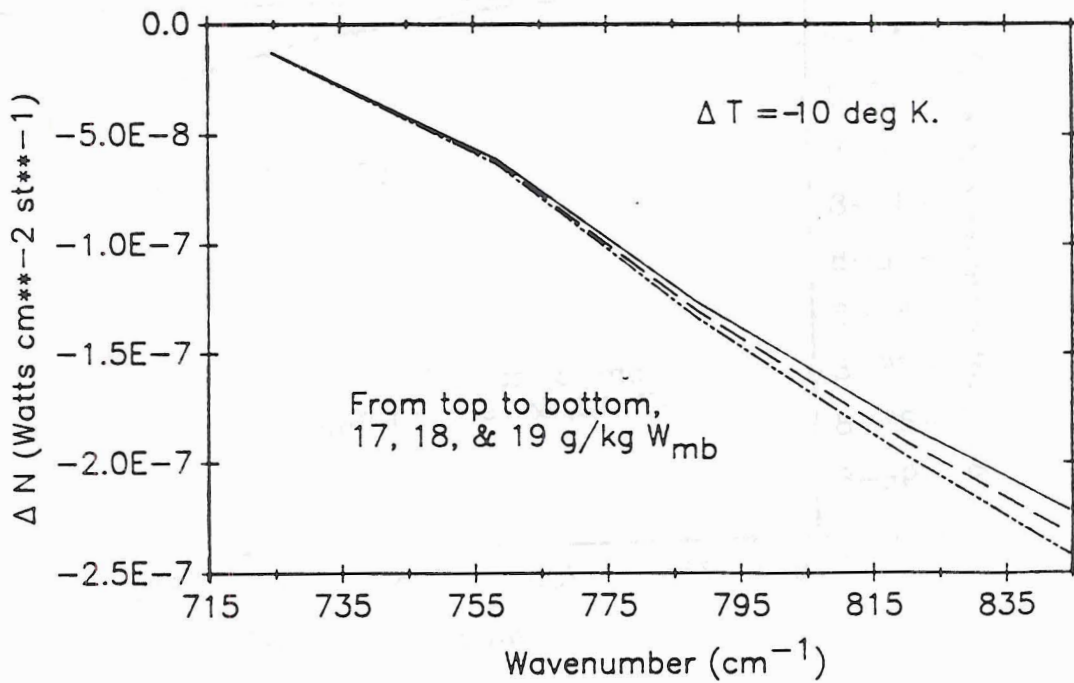
Figure 5.14: ΔN where atmospheric water vapor is 15 g/kg and the MB is loaded with 15, 18, and 19 g/kg water vapor. Microburst is centered at 5 Km and $\Delta T_{mb} = -10°$ K.
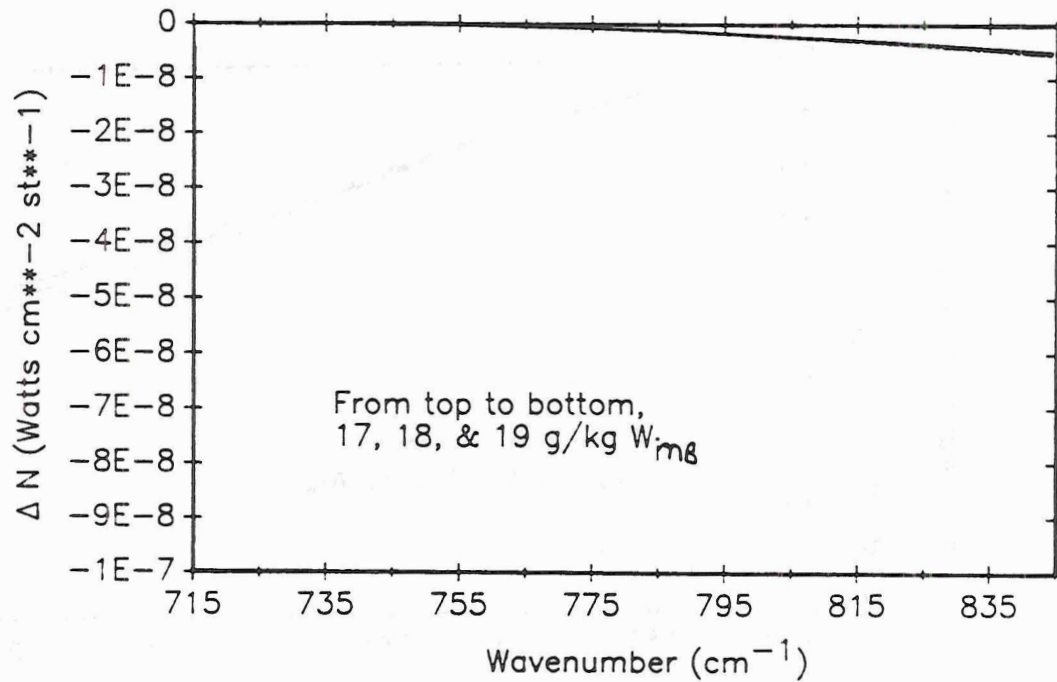
Figure 5.15: ΔN where atmospheric water vapor is 15 g/kg and the MB is loaded with 17, 18, and 19 g/kg water vapor. Microburst is centered at 10 Km $\Delta T_{mb} = -2°$ K.
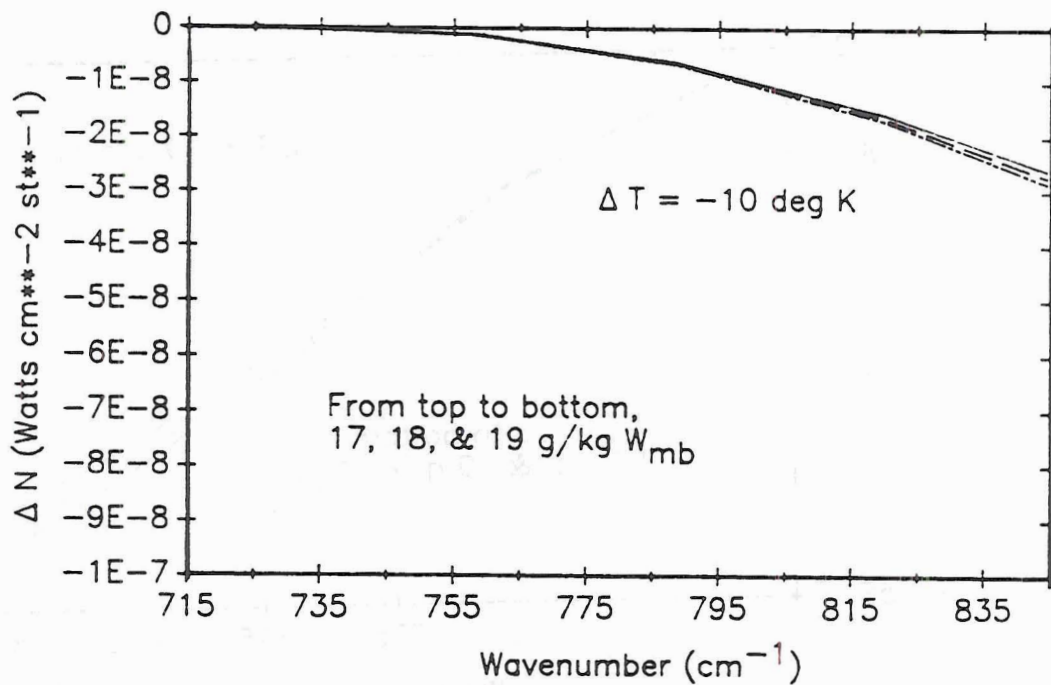
Figure 5.16: ΔN where atmospheric water vapor is 15 g/kg and the MB is loaded with 17, 18, and 19 g/kg water vapor. Microburst is centered at 10 Km $\Delta T_{mb} = -10°$ K.

5.4 Microburst Temperature and Surface Outflow Winds

In this model study we have prescribed a ΔT by comparing a typical atmospheric temperature with a hypothetical MB temperature. In practical application of this sensing technique, a radiance value will be observed by the sensor, then a brightness temperature calculation performed in order to determine the actual temperature of the MB shaft (Sinclair and Kuhn, 1990). Once this temperature is known we can determine the approximate surface outflow wind magnitudes by following a flow diagram similar to that described in Figure 5.17. This represents the most operationally significant part of the MB analysis. Once an outflow wind is calculated, the pilot can make a determination as to whether or not an encounter might pose a risk to his aircraft.

In the following analysis many assumptions are made. Calculated average outflow winds ($\overline{u}$) are considered to be gross approximations of actual outflow winds. Nevertheless, because the following algorithm is based on well established dynamic and thermodynamic principles, we feel that it will yield accurate enough results to be meaningful to an aircrew. Also, as the meteorological community accumulates more data on MBs, this procedure can be fine tuned to give even more accurate results.

Blocks 1 and 2 represent the radiance received from scans of the MB atmosphere and the ambient atmosphere respectively. ΔN at aircraft altitude z_a is calculated in Block 3 in the same manner as done in this chapter (during a MB scan). At some point in our range scan we are able to calculate the MB shaft temperature T_{mb} (Block 4) and then calculate ΔT. For simplicity, ΔT is constant and assumed independent of height. Block 5 represents environmental temperature as a function of height, and is approximated at cloud base by using the temperature at the airplane and assuming a dry adiabatic lapse rate below cloud base. Cloud base altitude must be known. Initial microburst vertical motion at cloud base (w_{cb}) is an assigned value of -1 m s^{-1}.

Knowing a value for ΔT, and having a function defining T at all levels, the vertical momentum equation is used to calculate vertical momentum (w) at the top of the MB outflow layer (Block 6). Block 7 is the Boussenesque form of the continuity equation

and allows calculation of divergence in the outflow layer. This assumes a flat, frictionless surface and that divergence is independent of height.

Finally, if we assume that divergence is constant in the outflow layer, and use the definition of divergence in cylindrical coordinates, we can solve for $\bar{u}$ as a function of radius. Preliminary calculations using this technique seem to compare favorably with actual near surface measurements of MB outflows during both the JAWS and NIMROD experiments (Fujita, 1985). Improved parameterization would enable a similar technique to become part of the actual IR scanning algorithm aboard an aircraft.
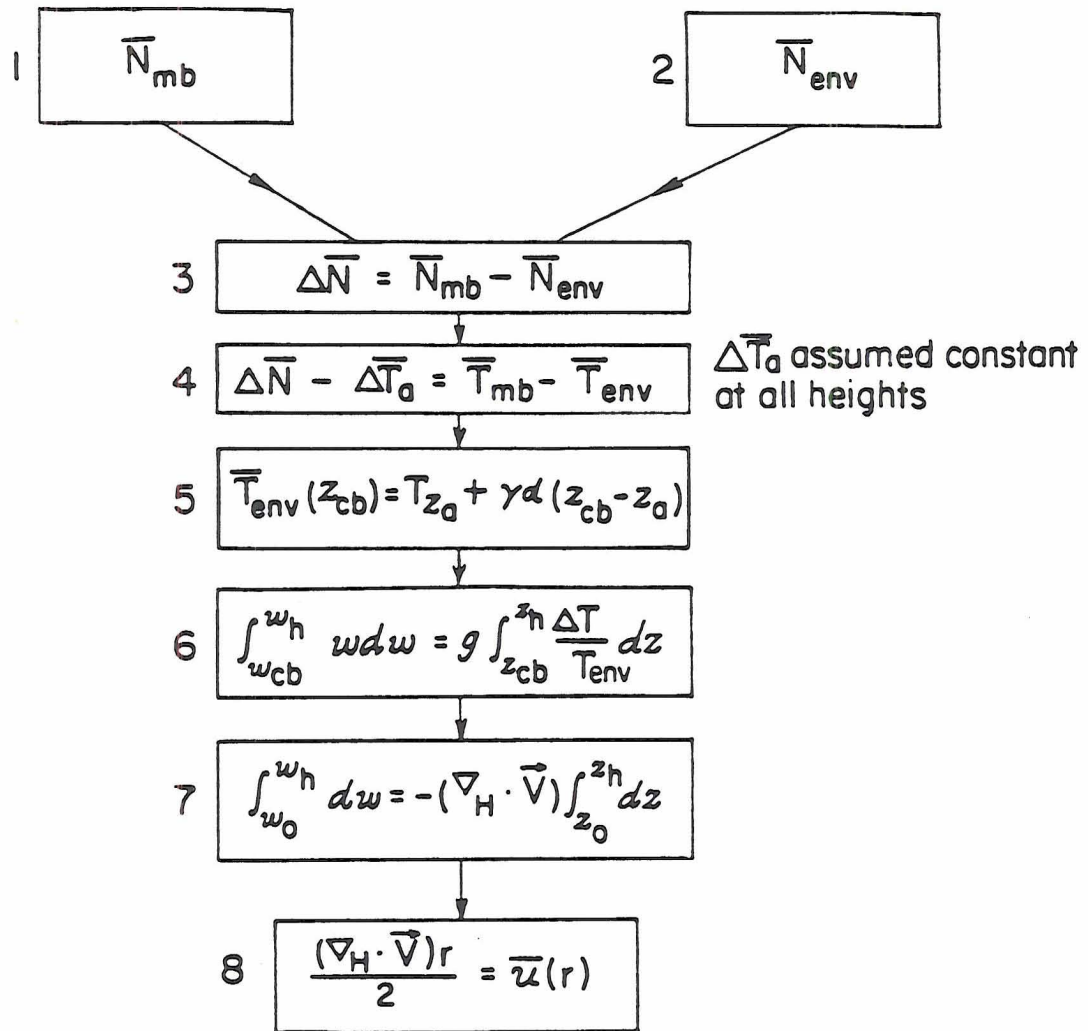
Figure 5.17: Flow diagram for calculation of near-surface winds. This algorithm illustrates a possible means to calculate approximate MB outflow winds when initial ΔN values are sensed by a detector at flight level z_a (see text).

1. $\overline{N}_{mb}$

2. $\overline{N}_{env}$

3. $\Delta \overline{N} = \overline{N}_{mb} - \overline{N}_{env}$

4. $\Delta \overline{N} - \Delta \overline{T}_a = \overline{T}_{mb} - \overline{T}_{env}$ $\Delta \overline{T}_a$ assumed constant at all heights

5. $\overline{T}_{env}(z_{cb}) = T_{sa} + \gamma_d(z_{cb} - z_{sa})$

6. $\int_{z_{cb}}^{z_{it}} g \frac{\Delta \overline{T}}{\overline{T}_{env}} dz$ and/or $g \frac{\Delta \overline{T}}{\overline{T}_{env}} \frac{z_{it}}{z_{cb}}$

7. $\int_{z=0}^{z_{it}} dz = -(\nabla_H \cdot \overline{V}) \int_{z=0}^{z_{it}} dz$

8. $\frac{g}{2} \nabla_H \overline{V}_H^2 = \overline{V}_g^2(r)$

Figure 3.17: Flow diagram for calculation of near-surface winds. This algorithm illustrates a possible means to calculate approximate MD outflow winds when initial ΔV values are forced to a definite at flight level z_1 [see text]

Chapter 6

SUMMARY AND CONCLUSIONS

The purpose of this work was to develop an infrared scanning scheme for the indirect detection and ranging of low level wind shear (LLWS). In particular, this study examines LLWS as produced by the microburst phenomena (Fujita, 1985). A computer aided radiometric analysis was conducted of various microburst atmospheres in an effort to show that infrared detection of microbursts was possible using currently available infrared equipment. Along with this objective an attempt was made to apply a weighting function scheme in order to determine an actual range to our modeled microburst. Microburst atmospheres were modeled to represent two areas: the High Plains of the U.S. and the more moist environment of the south eastern United States.

A radiative transfer model was built to compare the radiance received from an ambient atmosphere to that radiance received from a microburst embedded in the same atmosphere. Since a microburst shaft is colder than the ambient atmosphere, these two radiance measurements will differ from one another based on the thermal qualities of the microburst. If this arithmetic radiance difference (ΔN) is above some pre-determined hazard threshold, then the presence of a microburst can be deduced and LLWS inferred. In this study, we have utilized the 12 - 15 μ wing of the 15μ CO_2 absorption band where CO_2 and H_2O vapor are the only significant atmospheric absorbers.

This technique scans an azimuthal sector ahead of the aircraft and calculates a ΔN at numerous selected wavenumber locations. The microburst atmosphere is scanned in horizontal range by changing these instrument channels (wavelength of observation). By selecting these various channels, we are able to adjust the physical range at which a maximum amount of radiation is received at a theoretical sensor. This represents a weighting

function ranging scheme. In this technique, the radiance deficit produced by a microburst is most clearly depicted when it is physically co-located where a weighting function peaks in magnitude. When this co-location occurs in the scan, a maximum calculated ΔN is the result. This maximum ΔN value, based on the location of a known weighting function peak, should then represent the physical range of the observed microburst. In order to minimize the width of the calculated weighting functions, we used a narrow bandwidth of 1 cm^{-1}. This provides a relatively discrete weighting function resulting in better range resolution.

Model results indicate that microburst detection with this method can be accomplished using currently available infrared sensor technology. Sensor with a sensitivity of $\approx$ 4×10^{-8} W cm^{-2} str^{-1} would be adequate to sense most all of our modeled microbursts. Liquid cooled mercury-cadmium-telluride detectors have detectivities ($D^{*} = 10^{10} - 10^{11}$ cm $hz^{\frac{1}{2}}/W$ for detection of signals as low as 10^{-8} to 10^{-9} W cm^{-2} str^{-1} (Sinclair and Kuhn, 1990).

The success of the microburst range determination using the weighting function technique depended on the moisture distribution in the microburst and the environment. In the relatively dry conditions of the high plains atmosphere, we were able to accurately determine the range of a microburst at 5 km when the ΔT of the microburst was only $-2°$ K. As we increased ΔT to $-10°$ K, transmission values through the microburst decreased significantly causing the identifiable peak in calculated ΔN values to shift toward higher wavenumbers (lower frequencies).

By analyizing typical microburst characteristics, we were able to determine that colder microburst temperatures, coupled with water loading effects, cause drastic transmissivity decreases in the modeled atmospheres. These transmittance decreases can act to alter pre-calculated weighting functions by changing the physical location at which the weighting functions peak. This introduces uncertainties about the actual microburst range using the proposed ΔN technique.

Lower infrared transmissivities found in the more moist atmospheres of the south-east United States do not allow pre-determined weighting functions to peak at large distances

from the sensor. Under these more moist conditions, microburst detection and ranging are limited to distances relatively close to the sensor ($x \leq 4$ Km) as the radiance deficit produced by the microburst is heavily attenuated before reaching the theoretical radiometer. These shorter distances however, still provide sufficient warning of microburst presence and location estimates.

Our work has shown that although we can detect these microbursts, the proposed ranging technique needs more study to become useful for a wide spectrum of realistic microburst atmospheres. Variations of atmospheric water vapor and temperature act to alter the ranging capabilities of pre-determined weighting functions.

A limiting factor in this study is the lack of adequate field data with which to parameterize our model. Complete airborne studies of both wet and dry microbursts are necessary to provide the data base needed for comprehensive modeling. At present, only sparse information is available on the water loading and temperature structure of high plains microbursts (Sinclair and Kuhn, 1990), and no detailed information is available on the more moist variety of microbursts. Information on the characteristics of mid to upper level microburst structure would also provide more insight on precursors which may lead to better nowcasting of these microbursts.

Further evaluation of this technique could yield a scanning algorithm that would locate the microburst based on the gradient of radiance received. This technique could prove very useful for detection in the more moist atmospheres. It is also possible that other scanning schemes could be incorporated into our method to further delineate the microburst radiance anomaly.

Perhaps the ΔN technique would work well in a different part of the electromagnetic spectrum. Since water vapor (and clouds) are limiting constraints in the 15μ region, we may be able to successfully apply this technique on the wings of the 118 GHz O_2 absorption band where this water contamination is not a problem. Other areas of the spectrum could also be considered.

Other applications can benefit from a similar ranging technique. There is currently much interest in the detection of stratospheric clear air turbulence (CAT) ahead of high

speed aircraft. At these altitudes, the relatively dry atmosphere makes it possible to use a similar method in pinpointing turbulence believed to be associated with the high altitude influx of moist tropospheric air (Kuhn, *et al.*, 1977, and Kuhn,*et al.*, 1978). In this application, water vapor acts more as a source than an atmospheric filter. Kuhn,*et al.*, (1978) have show with this technique that at altitudes between 15,000 and 45,000 feet, CAT alerts range from 1.5 to 6.0 minutes ahead of an actual aircraft encounter.

In this analysis of a simple, low cost LLWS detector we have gained a more complete understanding of atmospheric radiative processes that occur in this region of the spectrum. Although there are still some uncertainties concerning our discrete ranging capabilities, the problems do not look insurmountable. With further development this method could be effective in detecting and locating microbursts either as a stand alone system or as a supplement to another pre-existing network. This work represents an important step in the development of an airborne infrared microburst detection and ranging technique.

REFERENCES

Bedard, A.J. Jr.,*et al.*, 1979: A thunderstorm gust-front detection system: Part 1, System operation and significant case studies and Part 2: Statistical results, FAA Report No. FAA-RD-79-55. Federal Aviation Administration, Washington D.C.

————, J. McCarthy, and T. Lefebvre, 1984: Statistics from the of the low-level wind shear alert system (LLWAS) during the joint airport weather studies (JAWS) project, Interim Report DOT/FAA/PM- 84/132, December.

Burch, D.E., and D.A. Gryvnak, 1980: Continuum absorption by H_2O vapor in the infrared and millimeter regions, " Atmospheric Water Vapor ", New York, Academic Press, 47-76.

Campbell, S.D., 1989: Use of Features Aloft in the TDWR Microburst Recognition Algorithm, Preprints, 24rd Conf. on Radar Meteorology, AMS, Tallahassee, Fl, 167-170.

Caracena, F., P.M. Kuhn, and R.L. Kurkowski, 1981: Design and preliminary tests of an IR-airborne LLWS remote sensing system, AIAA Paper 81- 0239, January.

————, R.A. Maddox, J.F.W. Purdom, J.F. Weaver, R.N. Green,1983: Multi- scale analysis of meteorological conditions affecting Pan American World Airways Flight 759, NOAA Technical Memorandum ERL ESG-2, Environmental Sciences Group, Boulder, CO, January.

Chandrasdkhar, S.,1960: "Radiative Transfer", New York, Stellar Publications.

Clough, S.A., F.X. Kneizys, R. Davies, R.Gamache and R. Tipping, 1980: Theoretical line shape for H_2O vapor; application to the continuum, "Atmospheric Water Vapor", New York, Academic Press, 25-46.

————, Merritt, M.W., and J.T. DiStefano, 1989: Microburst Recognition Performance of TDWR Operational Testbed, Preprints; 3rd International Conference on the Aviation Weather System, Anaheim, Calif., 25-30.

Eilts, M.D., 1986: Low Altitude Wind Shear Detection with Doppler Radar, *J. of Clim. and Appl. Meteor.*, Vol. 26, 96-106.

Elachi, C., 1987:" Introduction to the physics and techniques of remote sensing", John Wiley and Sons, New York.

Elsasser, W.M., and J.E. King, 1952: Principles of Radiative Transfer in Far Infrared Atmospheric Bands, Air Force Cambridge Research Center, Bedford, MA. Contract no. AF 19(122)-392.

Fawbush, E.J., and R.C. Miller, 1954:A basis for forecasting peak wind gusts in non-frontal thunderstorms, *Bull. Amer. Meteor. Soc.*,35, 14-19.

Federal Registry, 1988: Airborne low-altitude wind shear equipment and training requirements, Volume 53, No.187, Rules and Regulations. p.37688, Department of Transportation, FAA, 14CFR Parts 121 and 135 [DOCET 19110: Amendment Nos. 121-149, 135-27].

Fleming H.E., and L.M. McMillin, 1977: Atmospheric transmittance of an absorbing gas. 2: A computationally fast and accurate transmittnace model for slant paths at different zenith angles, *Appl. Opt.*, 16, No. 5, 1366-1370.

Fujita, T.T., and H.R. Byers, 1977: Spearhead Echo and Downburst in the crash of an airliner, *Mon. Wea. Rev.*, 105, 129-146.

—————, and R.M. Wakimoto, 1983: Microbursts in JAWS depicted by Doppler radars, PAM, and aerial photographs, Preprints 21st Conf. on Radar Meteor., Edmonton, Canada, Amer. Meteor. Soc., 638-645.

—————, 1985:" The Downburst; Microburst and Macroburst", University of Chicago, SRMP, University of Chicago.

—————, 1986:" DFW Microburst on August 2, 1985", University of Chicago, SRMP, University of Chicago.

Foster , D.S., 1958: Thunderstorm gusts compared with computed downdraft speeds, *Mon. Wea. Rev.*, 86, (3).

Goff, R.C., 1980: The LOw Level Wind Shear Alert System (LLWAS), Final Report No. FAA-RD-80-45/FAA-NA-80-1, US Department of Transportation, FAA, Washington, D.C.

————, and R.H Gramzow, 1989: The Federalk Aviation Administration's Low Level Windshear Alert System: A Project Management Perspective, Preprints; 3rd International Conference on the Aviation Weather System, Anaheim, Calif., 408-413.

Goody, R.M., 1964:" Atmospheric Radiation I; Theoretical Basis", Oxford, Clarendon Press.

————, and Y.L. Yung, 1989:" Atmospheric Radiation; Theoretical Basis, 2nd edition", Oxford University Press.

Gryvnak, D.A., and D.E. Burch, 1978: Infrared Absorption by CO_2 and H_2O, AFCRL, Hanscom Air Force Base, MA., Scientific Report AFGL-TR-78- 0154.

Hudson, R.D., 1969:" Infrared System Engineering", New York, John Wilson and Sons.

Kidder, S.Q., and T.H. Vander Haar," Satellite Meteorology; An Introduction", Academic Press, to be published.

Kneizys, F.X., E.P. Shettle, L.W. Aberu, J.H. Chetwynd, G.P. Anderson, W.O. Gallery, J.E.A. Shelby, and S.A. Clough, 1988: Users Guide to LOWTRAN7, Air Force Geophysics Laboratory, Hanscom Air Force Base, MA. AFGL-TR-88-0177.

Kuhn, P.M., F. Caracena, and C.M. Gillespie, Jr., 1977: Clear air turbulence: Detection by Infrared observations of water vapor, Science,196, 1099-1100.

————, I.G. Nolt, I.P. Stearns, and J.V. Radostitz, 1978: Infrared bandpass for clear-air detection, Optics Letters,3, No. 4, 130- 133.

————., and R.L. Kurkowski, and F. Caracena, 1983: Airborne operation of an infrared low-level windshear predicition system, J. Aircraft,20, 170-173.

————, and R.L. Kurkowski, 1984: Airborne Infrared Low-altitude wind shear detection test, J. Aircraft, 21, 792-796.

Liou, K.N., 1980:" An Introduction to Atmospheric Radiation", New York, Academic Press.

Mahoney, W.P., and A.R. Rodi, 1987: Aircraft Measurements on Microburst Development from Hydrometeor Evaporation. *Bull. Amer. Meteor. Soc.*, Vol. 44, No. 20, 3037-3051.

McCarthy, J., and J. Wilson, 1985: The Classify, Locate and Avoid Wind Shear (CLAWS) Project at Denver's Stapleton International Airport: Operational testing of terminal weather hazard warnings with an emphasis on microburst wind shear. Preprints, 2nd Int'l Conf. on the Aviation Weather System, Montreal, Canada. Amer. Meteor. Soc., 247-256.

McClatchy, R.A., and J.E.A. Selby, 1972: Atmospheric Transmittance, 7-30 μ: Attenuation of CO_2 Laser Radiation, Air Force Geophysics Laboratory, Hanscom Air Force Base, MA. AFCRL-72-0611.

——————, R.W. Fenn, J.E.A. Selby, F.E. Voltz, and J.S. Garing, 1973: Optical Properties of the Atmosphere: Third Edition, Air Force Cambridge Research Laboratory, Bedford, MA. Project 7670, AFCRL-72-0497.

National Research Council, 1983:" Low Altitude Windshear and Its Hazard to Aviation". National Academy Press, Washington, D.C., 161pp.

Nordstrom, R.J., and M.E. Thomas, 1980: The Water Vapor Continuum as Wings of Strong Absorption Lines," Atmospheric Water Vapor", New York, Academic Press, 77-100.

NTSB, 1983:Aircraft Accident Report– Pan American World Airways, Clipper 759, N4737, Boeing 727-235, New Orleans International Airport, Kenner, Louisiana, July 9, 1982. NTSB/AAR-83/82, National Transportation Safety Board, Washington, D.C., 115p.

Oak Ridge National Laboratory, 1989: Atmospheric CO_2 concentrations: personal communication, December.

Proctor, F.H., 1989: A relationship between peak temperature drag and velocity differential differential in a microburst. Third International Conference on Aviation Weather Systems, Anaheim, CA, Amer. Meteor. Soc, Boston, Feb 3.

Rodi, A.R., F.M. Remer, and R.M. Rasmussen, 1986: Aircraft and radar observations of downdraft formation by evaporation and melting of hydrometeors. preprints, 23rd Conf. on Radar Meteor., Snowmass, Amer. Meteor. Soc., 93-96.

Rothman, L.S., A. Goldman, J.R. Gillis, R.R. Gamache, H.M. Pickett, R.L. Poynter, N. Husson and A. Chedin, 1983a: AFGL Trace gas compilation: 1982 version, *Appl. Opt.*, **22**, 1616.

————, R.R. Gamache, A. Barbe, A. Goldman, J.R. Gillis, L.R. Brown, R.A. Toth, J.M. Flaud, and C. Camy-Peyret, 1983b: AFGL Atmospheric line parameter compilation: 1982 edition, Appl. Opt., **22**, 2247.

Sinclair, P.C. and P.M. Kuhn, 1987: Forward looking airborne infrared wind shear sensor operation in precipitation. Final Report, to NOAA, Enviornmental Research Laboratory, Boulder, CO, September.

————, and P.M. Kuhn, 1990: Aircraft low level wind shear detection and warning system., accepted for publication, *J. Atmos. Sci.*

Smith, W.L., 1972: Satellite techniques for observing the temperature structure of the atmosphere, *Bull. Amer. Meteor. Soc.*, **53**, No.11, 1074-1082.

Smith, W.L., 1969: A Polynomial representation of Carbon Dioxide and Water Vapor Transmission, ESSA Technical Report, NESC 47, Environmental Science Services Center, National Environmental Satellite Center.

Smythe, G.R., 1989: Evaluation of the 12-station Enhanced Low Level Wind Shear Alert System (LLWAS) at Denver Stapleton International Airport. Preprints; 3rd International Conference on the Aviation Weather System, Anaheim, Calif. 41-46.

Srivastava, R.C., 1987: A model of intense downdrafts driven by the melting and evaporation of precipitation. *J. of Atmos. Sci.*, **44**, No. 13, 1752-1773.

Turnbull, D., McCarthy, J., Evans, J., and D. Zrnic, 1989: The FAA Terminal Doppler Weather Radar (TDWR) Program. Preprints; 3rd International Conference on the Aviation Weather System, Anaheim, Calif. 414- 419.

Wark, D.Q., and H.E. Fleming, 1966: Indirect measurement of atmospheric temperature profiles from satellites: 1. Introduction, *Mon. Wea. Rev.*, **94**, No. 6, 351-362.

Wilson, W.W., Roberts, R.D., Kessinger, C., and J. McCarthy, 1984: Microburst Wind Structure and Evaluation of Doppler Radar for Airport Wind Shear Detection, *J. of Clim. and App. Meteor.*, Vol. **23**, 898-915.

Appendix A

PREDICITION OF ATMOSPHERIC TRANSMISSION AND RADIANCE

Over the past 50 years various computer codes and empirical methods have been developed in attempts to accurately predict atmospheric transmittance and radiance. Three such schemes are investigated for the purpose of this study: the LOWTRAN7 and FAS-COD2 codes and for transmittance calculations only, the Smith Coefficient method.

Each of these schemes have benefits and drawbacks but all have been useful not only in producing accurate values, but in confirming the accuracy of each by comparison.

A.1 LOWTRAN7 (LOw resolution TRANsmittance code)

LOWTRAN7 is a low resolution propagation model and computer code for predicting atmospheric transmission and background radiance from 0 to 50,000 cm^{-1} at a fixed resolution of 20 cm^{-1} (Kneizys, et. al., 1988). LOWTRAN7 capabilities include calculations of scattered solar and lunar radiance, and direct solar calculations. The code also includes the effects of molecular scattering, aerosol extinction (both of which are neglected in our study), and continuum effects. Absorption and scattering by hydrometeors can also be calculated by the program. LOWTRAN7 has evolved from its early inception as the LOWTRAN code created in the early 1970's. It was developed and is maintained by the Air Force Geophysics Lab, Optical/Infrared Technology Division at Hanscom Air Force Base, Massachusetts. LOWTRAN7 can be used in a horizontal, vertical, or slant path mode and will accommodate user specified input data such as temperature, pressure and absorber amounts. It can also use default values from the 1976 U.S. Standard Atmospheres and other seasonally averaged profiles providing a total of 7 complete default atmospheres to choose from. Default atmospheres define temperature, pressure, density

ratios for H_2O, O_3, CH_4, CO, $CO2$, $O2$, and $N2O$ as a function of altitude. Also available in the code is a new atmospheric data base consisting of separate molecular profiles (0-100 km) for thirteen minor and trace gases. Refraction and earth curvature are considered in the calculation of the atmospheric slant path and attenuation amounts along the path as required. When used in the vertical or slant path mode, LOWTRAN7 calculates radiance/transmission amounts as temperature and pressure vary in the vertical. Horizontal measurements are limited to constant temperature and pressure calculations when LOWTRAN7 is used in its normal configuration.

The code uses a single parameter band model for molecular absorption (Goody and Yung, 1989). Single parameter band models calculate average absorption values over a finite interval where many absorption lines may exist. These line intervals (bands) assume a Lorentz or modified Lorentz line shape over the band-width of the model.

Since introduction in the LOWTRAN6 code, absorption by the water vapor continuum has been calculated after the method developed by Clough, $et.$ $al.$ (1980), where the continuum contribution to the absorption coefficient $\kappa_C(\nu)$, is given by the expression

$$\kappa_C(\nu) = \rho_s \nu \tan h(hC/2kT)\left[(\frac{\rho_s}{\rho_0})\tilde{C}_s(\nu,T) + (\frac{\rho_f}{\rho_0})\tilde{C}_f(\nu,T)\right]$$

where T is the temperature in deg K, ν is the wavenumber cm^{-1}, hC/k = 1.43897 deg $- K - cm$, $(\frac{\rho_s}{\rho_0})$ and $(\frac{\rho_f}{\rho_0})$ are the number density ratios for self and foreign continuum, and $\tilde{C}_s$ and $\tilde{C}_f$ are wavenumber dependent continuum absorption parameters for self and foreign broadening components. The quantities ρ_s and ρ_f are the densities of water vapor and of all other molecular species respectively; ρ_0 is the reference number density defined at 1013 mb and 296 deg K. Figures 4.2A and 4.2B show wavelength versus LOWTRAN7 transmittances for various absorber amounts along the indicated pathlengths. As illustrated, the dependence of transmission on water vapor content is substantial.

LOWTRAN7 has the disadvantage of a wide, fixed resolution. This is particularly limiting in our MB study as we are trying to create more discrete weighting functions by using a more narrow bandwidth for radiance calculations. However, this program has

been most useful in isolating individual absorber contributions in the atmosphere. By nature of the LOWTRAN7 output, it is possible to receive a itemized list of transmission contributions from each molecular absorber in the given atmosphere. This feature is shown in the graphed results of Figures 4.2A and 4.2B where the total atmospheric transmission is illustrated by the individual effects of each pertinent constituent.

A.2 FASCOD2 (FASt atmospheric signature CODe)

FASCOD2 is a high resolution model and computer code developed for the line-by-line calculation of transmittance and radiance with particular application to the earth's atmosphere. In FASCOD2, the absorption coefficients in very narrow spectral intervals are computed as sums of contributions from each of the absorption lines in the band then integrated over the atmospheric path. The transmittances for these narrow spectral intervals are convolved with the spectral response function of the instrument.

This Fortran program is applicable to spectral regions from the microwave to the visible and like LOWTRAN7 can accommodate user specified input or input values from various default profiles. The contribution from continuum absorption is included in this model in the same manner as LOWTRAN7. There are 3 algorithms for line shape functions to keep the errors due to differences in the far wings minimized. For our purposes, FASCOD2 will yield the same output results as LOWTRAN7 with the important difference of finer resolution.

Incorporated in FASCOD2 is the spectral absorption line data base HITRAN (Rothman, *et. al.*,1983a and Rothman,*et al.*, 1983b). This data base includes line-by-line absorption information for all common atmospheric gasses and for some trace gas constituents as well. This is the heart of the FASCOD2 program. The actual HITRAN data base contains over 60,000 lines of absorption data representing atmospheric line absorption from the microwave to the visible. A line file is created from this data base that allows the user to work with only that part of the HITRAN spectrum which applies to a specific segment of the electromagnetic spectrum. This way, absorption line information is more efficiently managed. In our case only the IR portion of the spectrum has been selected for a working line file.

FASCOD2 has the added capability of user defined resolution. This is an important feature as we can establish correct transmission values based on our weighting function requirements. This better resolution will enable us to narrow down the weighting function and better descretize our look distances. By using a bandwidth that is optimal in defining a sharp weighting function, and optimal for receiving input power at the sensor, we hope to be able to design an IR sensor that will more accurately locate the anomalous cold air associated with a microburst.

Because of the detail and completeness of the HITRAN database, FASCOD2 is extremely accurate and is considered the standard in much of the radiative transfer community. However, the name is somewhat misleading. The massive amount of calculations required for each program run make high speed use of FASCOD2 impractical if not impossible.

A.3   The Smith Coefficient Method

W.L. Smith (1969) developed an empirical model for characterizing H_2O and CO_2 transmission with a bandwidth/resolution of 5 cm^{-1}. This eight term polynomial model uses coefficients determined from calculated transmittances tabulated in 5 cm^{-1} intervals covering a spectral range from 507.5 to 797.5 cm^{-1}. Smith's coefficients for water vapor and CO_2 are input into a Fortran code where the transmittance is calculated by the following relations

$$\mathcal{T}_{\Delta \nu} = \exp\left[-\exp\left(W\right)\right] \tag{A.1}$$

where

$$W = \sum_{i=0}^{8} C_i A_i$$

and the C_i's are the H_2O and CO_2 coefficients. The coefficients are determined by fitting the above summation equation by least squares to a point by point calculation of transmittance. Variables A_0 thru A_8 are prescribed mathematically according to the temperature, pressure, and the absorber amounts considered. Since this is an empirical scheme, the

H_2O coefficients implicitly include both effects of water vapor lines and absorption due to the continuum.

This coefficient method was successfully modified by Fleming and McMillin, (1977). Smith's entire coefficient matrix can be customized to work within any specified spectral interval (bandwidth). This has important consequences for application to our on-board radiometer. When a spectral bandwidth is chosen, we should be able to create our own unique transmission program by computing our own tailored coefficients.

Integrated in the design of the detector will be a co-processor unit capable of calculating atmospheric transmittance based on temperature, pressure, and absorber amounts for a given pathlength. As brought out by this study, H_2O vapor and CO_2 are the two significant atmospheric absorbers in our wavelength study region.

Of the three methods described, a variation of the Smith coefficient method seems most suited for this purpose. Unlike LOWTRAN7 and FASCOD2, Smith's method uses less than 70 lines of Fortran code and is computationally fast. The Smith method is accurate and has been verified (Smith, 1969) to within approximately 1 percent of actual measured values.